

AD \_\_\_\_\_

Award Number: W81XWH-05-1-0363

TITLE: Miniature and Molecularly Specific Optical Screening Technologies for Breast Cancer

PRINCIPAL INVESTIGATOR: Nirmala Ramanujam, Ph.D.

CONTRACTING ORGANIZATION: Duke University  
Durham, NC 27708

REPORT DATE: October 2008

TYPE OF REPORT: Annual

PREPARED FOR: U.S. Army Medical Research and Materiel Command  
Fort Detrick, Maryland 21702-5012

DISTRIBUTION STATEMENT: Approved for Public Release;  
Distribution Unlimited

The views, opinions and/or findings contained in this report are those of the author(s) and should not be construed as an official Department of the Army position, policy or decision unless so designated by other documentation.

REPORT DOCUMENTATION PAGE				Form Approved OMB No. 0704-0188	
Public reporting burden for this collection of information is estimated to average 1 hour per response, including the time for reviewing instructions, searching existing data sources, gathering and maintaining the data needed, and completing and reviewing this collection of information. Send comments regarding this burden estimate or any other aspect of this collection of information, including suggestions for reducing this burden to Department of Defense, Washington Headquarters Services, Directorate for Information Operations and Reports (0704-0188), 1215 Jefferson Davis Highway, Suite 1204, Arlington, VA 22202-4302. Respondents should be aware that notwithstanding any other provision of law, no person shall be subject to any penalty for failing to comply with a collection of information if it does not display a currently valid OMB control number. <b>PLEASE DO NOT RETURN YOUR FORM TO THE ABOVE ADDRESS.</b>					
1. REPORT DATE 1 Oct 2008		2. REPORT TYPE Annual		3. DATES COVERED 1 Sep 2007 – 31 Aug 2008	
4. TITLE AND SUBTITLE  Miniature and Molecularly Specific Optical Screening Technologies for Breast Cancer				5a. CONTRACT NUMBER	
				5b. GRANT NUMBER W81XWH-05-1-0363	
				5c. PROGRAM ELEMENT NUMBER	
6. AUTHOR(S)  Nirmala Ramanujam, Ph.D.  E-Mail: <a href="mailto:nimmi@duke.edu">nimmi@duke.edu</a>				5d. PROJECT NUMBER	
				5e. TASK NUMBER	
				5f. WORK UNIT NUMBER	
7. PERFORMING ORGANIZATION NAME(S) AND ADDRESS(ES)  Duke University Durham, NC 27708				8. PERFORMING ORGANIZATION REPORT NUMBER	
9. SPONSORING / MONITORING AGENCY NAME(S) AND ADDRESS(ES) U.S. Army Medical Research and Materiel Command Fort Detrick, Maryland 21702-5012				10. SPONSOR/MONITOR'S ACRONYM(S)	
				11. SPONSOR/MONITOR'S REPORT NUMBER(S)	
12. DISTRIBUTION / AVAILABILITY STATEMENT Approved for Public Release; Distribution Unlimited					
13. SUPPLEMENTARY NOTES					
14. ABSTRACT  The goal of this proposal is to harness the power of light to create "miniature and molecularly specific optical technologies" for breast cancer diagnosis and detection. The miniature technologies will leverage on millimeter scale silicon detectors and LEDs to make compact devices that can be used in a practical clinical setting for breast cancer detection. The features that will be exploited for optical detection/diagnosis of breast cancer will include the physiological, structural and molecular alterations that accompany the transformation of a cell from a normal to malignant state. This proposal also focuses on using contrast agents, specifically aminolevulinic acid (ALA) induced protoporphyrin IX (PpIX) and NBDG, for the molecular detection of breast cancer.					
15. SUBJECT TERMS optical, spectroscopy, imaging, fiber-optic, molecular, screening					
16. SECURITY CLASSIFICATION OF:			17. LIMITATION OF ABSTRACT	18. NUMBER OF PAGES	19a. NAME OF RESPONSIBLE PERSON
a. REPORT	b. ABSTRACT	c. THIS PAGE			USAMRMC
U	U	U	UU	33	19b. TELEPHONE NUMBER (include area code)

**Table of Contents**

---

<b>INTRODUCTION</b>	<b>4</b>
<b>BODY PROJECT 1</b>	<b>4</b>
<b>BODY PROJECT 2</b>	<b>17</b>
<b>KEY RESEARCH ACCOMPLISHMENTS</b>	<b>30</b>
<b>REPORTABLE OUTCOMES</b>	<b>31</b>
<b>CONCLUSIONS</b>	<b>31</b>
<b>REFERENCES</b>	<b>32</b>

---

## 1. INTRODUCTION

The objective of this proposal is to harness the power of light to create “miniature and molecularly specific optical technologies” for the eradication of breast cancer. Specifically this application focuses on a system on a chip device to detect molecularly specific sources of optical contrast for breast cancer. Both intrinsic (hemoglobin saturation, total hemoglobin content, reduction-oxidation ratio) and extrinsic sources of optical contrast (specifically aminolevulinic acid (ALA) induced protoporphyrin IX (PpIX) and 2-[*N*-(7-nitrobenz-2-oxa-1,3-diazol-4-yl)amino]-2-deoxy-D-glucose (2-NBDG) will be studied for breast cancer imaging. These sources of contrast coupled with the system on a chip device will be initially used for intraoperative margin assessment and predicting/evaluating response to therapy. . Once we have established the feasibility of using this technology in the margin assessment and therapy application, we will focus on applications that focus on early detection, including core needle biopsy and ductoscopy, which require further modifications to the technology.

### 2.1 Project 1: System-on-a-chip device

#### A. Original SOW for five years

- 1) *To establish the design specifications of the first-generation system-on-a-chip device.* This aim will involve throughput calculations and Monte Carlo modeling to determine the signal-to-noise ratio that can be achieved with the nano scale sources and detectors, and the experimental evaluation of the signal-to-noise of the test system on turbid “tissue-like” media. The signal-to-noise ratios achieved with the test system will be quantitatively compared to that achieved with a standard bench top system (year 1).
- 2) *To engineer and test the first-generation system-on-a-chip device.* The knowledge base derived from aim 1 will be used to engineer a first generation system-on-a-chip device and the performance of the device will be characterized on synthetic tissue phantom models. The signal-to-noise ratio and fluorescence attenuation characteristics of the system-on-a-chip device will be compared to that of a standard bench top counterpart (year 2).
- 3) *To experimentally establish the signal-to-noise ratio with which the system-on-a-chip device can measure the fluorescence of ex vivo human breast tissues.* The system-on-a-chip device will be used to measure the fluorescence properties of 25 pair of malignant and non-malignant breast tissues excised from approximately 25 patients undergoing breast cancer surgery. The results obtained from this study will be quantitatively compared to benchmarks established by our bench top counterpart, which has been shown to measure breast tissue fluorescence with excellent signal-to-noise ratio (year 3).
- 4) *To test the feasibility of implementing optical spectroscopy via a ductoscope.* The system-on-a-chip device will be incorporated into a standard ductoscope. The ductoscope will be used to measure the fluorescence properties of 25 pair of malignant and non-malignant breast tissues excised from approximately 25 patients undergoing breast cancer surgery (years 4-5).

#### B. Summary of accomplishments in year 1

In year 1, we have completed the main goals of the SOW for year 1. The major achievements include thermal modeling of the heat dissipation effects of compact LEDs on tissue samples, selection of multi-wavelength compact light sources, calculating bandwidth effects of broadband light sources (such as LEDs) on the RMS errors for the extracted tissue optical and physiological properties, selection of photodiodes, and the design and testing of various single-pixel probe prototypes (P1 and P2 as shown in Figure 2.1). The major deviation from the SOW is that we used commercially available light sources and detector in our design, instead of using nano scale sources.

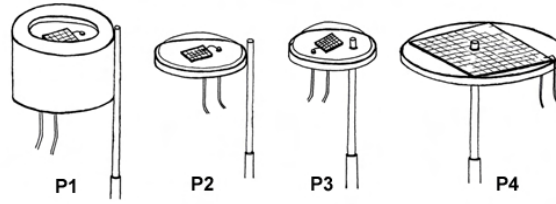


Figure 2.1. Conceptual drawings of four single-pixel probe geometries P1-P4.

### C. Summary of accomplishments in year 2

In year 2, we used knowledge base derived from year 1 to build more first generation single-pixel devices using an optical fiber for illumination and photodiodes for the collection of diffusely reflected light from a tissue sample. In particular, we have built single-pixel probes of different illumination and detection geometries named as P3-1 (600  $\mu\text{m}$  fiber), P3-2 (1 mm fiber), P4-1 (600  $\mu\text{m}$  fiber), and P4-2 (1 mm fiber), as shown in Figure 2.1, all using and 2.4 mm photodiode. P3-1 and P3-2 were tested in synthetic tissue phantoms with known optical properties, and their experimental diffuse reflectance spectra were compared with those of a forward Monte Carlo model.

We have also extracted the phantom optical properties from the diffuse reflectance spectra obtained from a tunable light source using an inverse Monte Carlo (MC) model. For P3-2, we found that the overall errors for quantifying the absorption and scattering coefficients were  $6.0 \pm 5.6\%$  and  $6.1 \pm 4.7\%$ , respectively. These results are comparable with those achieved with our bench-top system which has an overall error  $5.8 \pm 5.1\%$  and  $3.0 \pm 3.1\%$  for extracting  $\mu_a$  and  $\mu_s$ , respectively. A short paper on P3-2 has been accepted for publication by the Journal of Biomedical Optics Letters [1] and a copy of the manuscript is attached to this report. Phantom optical properties with reduced number of wavelengths were also extracted and compared to that of the bench-top system with all wavelengths.

In year 2, a clinical study conducted by our group using the bench-top system and the MC model showed that DRS alone has achieved comparable sensitivity and specificity for discriminating malignant from nonmalignant breast tissues as combined reflectance and fluorescence spectroscopy[2]. Therefore, our research in this miniature device has been focused mainly on diffuse reflectance spectroscopy (DRS) for breast cancer diagnosis and tumor margin assessment.

### D. Summary of accomplishments in year 3

In year 3, we have modified the probe geometries of the single-pixel probe developed in year 2 in order to increase the signal-to-noise ratio of the probe and to be able to extract a much larger range of optical properties than those of the probes built in year 2. The new probe was tested in synthetic tissue phantoms over a wide range of absorption and reduced scattering coefficients, and the phantom optical properties were extracted from the diffuse reflectance spectra obtained from the tunable light source and new probe with the inverse MC model previously developed by our group. Using the same phantom data collected by our new probe, optical properties with a reduced number of wavelengths were extracted to assess the feasibility of replacing the tunable light source with several smaller LEDs to further reduce the size and cost of the current system. In addition, cross-talk analysis was performed as a first step to multiplex the single pixel system into an imaging system that can quantify tissue physiological and morphological properties over a large tissue area. We have also fabricated a 3x3 fiber-photodiode array for test in the lab.

Although the original goals of the SOW is to use the system-on-a-chip device to measure the fluorescence properties of 25 pair of malignant and non-malignant breast tissues excised from approximately 25 patients undergoing breast cancer surgery, we understand that many challenges exist and it may take a relatively long time to reach this goal. As an intermediate step, the work in year 3 has been focused on partially miniaturizing the current bench-top system. This miniaturized probe preserves the potential for multiplexing that can be used for spectral imaging of tissue while uses all the wavelengths available to the bench-top system.

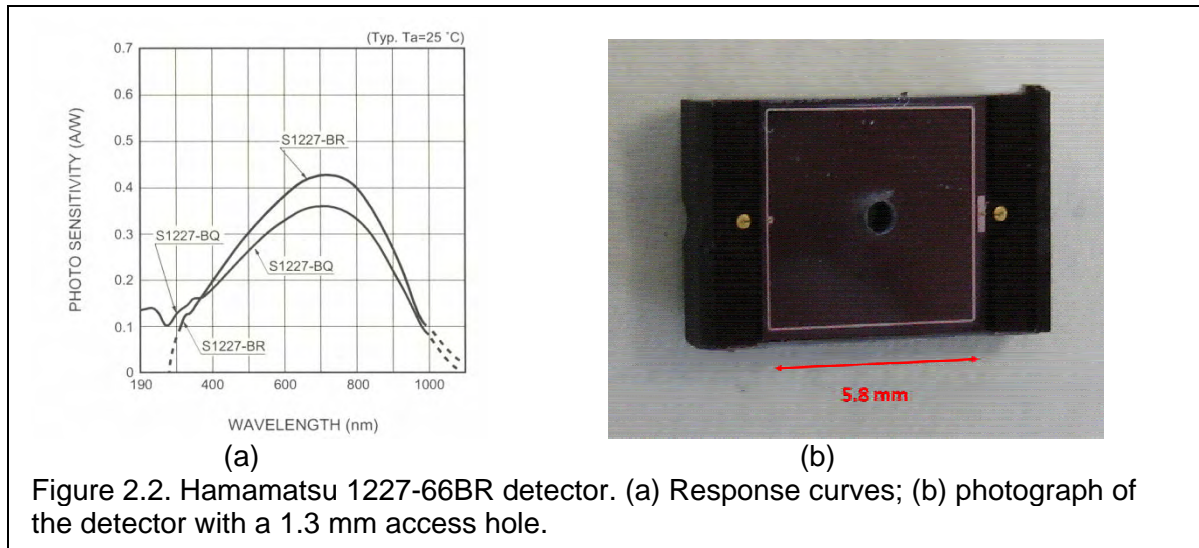
In year 3, a poster on the single-pixel device titled “A Miniature Optical Device for Noninvasive, Fast Characterization of Tumor Pathology,” was presented to the 2008 OSA Topic Meeting in Biomedical Optics, March 16-19, 2008, St. Petersburg, Florida. Manuscripts are also in final preparation for Optics Express and Journal of Biomedical Optics Letters.

### **2.1.1. Optical spectral imaging system based on tunable source and silicon detector**

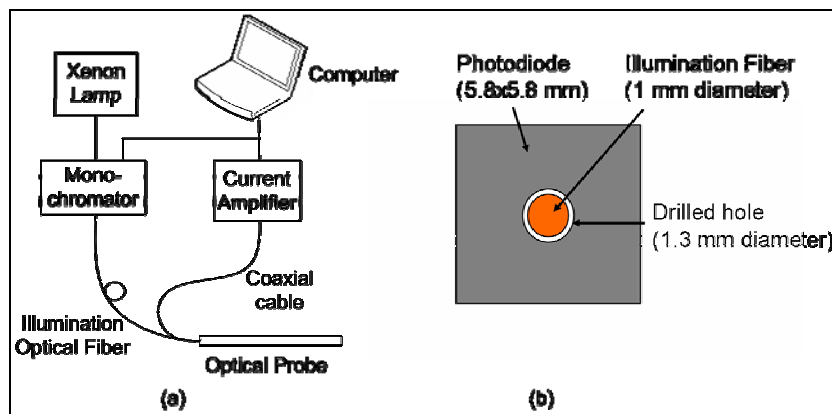
The first step towards the long-term goal of developing a compact spectral imaging device that can survey multiple points simultaneously is to design and build a spectral imaging system based on a tunable light source, similar to that in the current bench-top system, but silicon photodiodes to replace the expensive and bulky imaging spectrograph and CCD camera as well as the collection fibers. This section describes our progresses on the tunable source based spectral imaging system in year 3.

#### **A. Redesigned single-pixel probe and fabrication**

In year 2, we designed and tested single-pixel probes P3-1 and P3-2, which have 2.4x2.4 Hamamatsu S1226 detectors with an edge trimmed and a 1 mm diameter fiber adjacent to the detector. We found that while this previous probe was able to extract optical properties with relatively good accuracy compared to that of the bench-top system, it was only able to measure very little signal in phantoms with high absorption coefficients, wavelength averaged  $\mu_a = 2 \text{ cm}^{-1}$  over 400-600 nm, and no signal at all for  $\mu_a = 3.5 \text{ cm}^{-1}$  over 400-600 nm. To minimize the separation between the illumination and detection and to maximize the collection efficiency, a 5.8x5.8 mm photodiode (S1227-66BR, Hamamatsu) with enhanced visible and near-UV (Figure 2.2(a)) was selected to replace the S1126 detector used for P3-2. The resin encapsulation of the S1227-66BR allows for the formation of optical fiber access. Access was formed by the mechanical drilling of a 1.3 mm diameter hole in the center of the active area using diamond-coated drill bits (Figure 2.2(b)).



A single optical fiber with a core diameter of 1 mm and numerical aperture of 0.22 was fitted through the hole to illuminate the sample. The fiber was glued to the detector with transparent epoxy. The photodiode is connected to a current amplifier via a coaxial cable for diffuse reflectance measurements. This new probe is named P4-3 and schematics of the system and probe are shown in Figure 2.3.



## B. Single-pixel probe characterization

Our goal is to modify the bench-top system to decrease its size and cost of while still achieving comparable performance in extracting tissue optical properties. The modification of the bench-top system not only impacts size and cost but also the ability to seamlessly multiplex the device into a quantitative spectral imaging system. We compared throughput-related parameters and system characteristics of the original bench-top system with the modified system using the newly designed probe. The comparisons are enumerated in Table 2.1.

Table 2.1. Comparison of throughput-related parameters of original and modified systems

	Original System	Modified System
--	-----------------	-----------------

<b>Illumination Sources</b>	Xenon lamp and Monochromator (Reflectance and Fluorescence)	Xenon lamp and Monochromator (Reflectance only)
<b>Illumination Effective Area</b>	0.60 mm <sup>2</sup>	0.85 mm <sup>2</sup>
<b>Illumination NA</b>	0.22	0.22
<b>Detection Areas</b>	2.26 mm <sup>2</sup>	32.31 mm <sup>2</sup>
<b>Detection NA</b>	0.22	0.96
<b>Sensing depth</b>	0.5 - 2 mm	0.3 - 1.5 mm
<b>Detector QE</b>	35% (400~600 nm) Min: 26% @ 450 nm Max: 45% @ 600 nm	73% (400~600 nm) Min: 62% @ 400 nm Max: 79% @ 600 nm
<b>Dark Noise</b>	8.4 x 10 <sup>-5</sup> pA	5 pA
<b>Readout Noise</b>	4.2 x 10 <sup>-9</sup> A	1 x 10 <sup>-12</sup> A
<b>Average SNR (400~600 nm)</b>	34 dB	46 dB
<b>Cost of Detection System</b>	> \$20,000	< \$1,000

### C. Single-pixel probe experiments

To assess the performance of the single-pixel probe for measuring tissue optical properties, a series of experiments were performed on homogeneous liquid phantoms with  $\mu_a$  and  $\mu_s'$  similar to those of human breast tissue in the 400-600 nm wavelength range. Water soluble hemoglobin (H0267, Sigma Co., St. Louis, MO) and 1- $\mu$ m diameter polystyrene spheres (07310-15, Polysciences, Inc., Warrington, PA) were used as the absorber and scatterer, respectively, to create the synthetic tissue phantoms. Four sets of liquid phantoms were created and measured. The first set (S1) consisted of five phantoms of low range of concentrations (2-11  $\mu$ M) of the absorber and a fixed low number for scattering. The second set (S2) consisted of five phantoms of the same variable concentrations of Hb as S1, but with a fixed high number for scattering. The low and high scattering phantoms had a wavelength averaged  $\mu_s'$  of 11-13 cm<sup>-1</sup> and 20-22 cm<sup>-1</sup> over 400-600 nm, respectively. S1 and S2 were created for the purpose of comparing the performance of the new probe with the probe (P3-2) tested in year 2. So, the optical properties of phantom sets



S1 and S2 were similar to those used in the studies of year 2. Most notably, the averaged absorption coefficients over 400-600 nm do not exceed  $2.5 \text{ cm}^{-1}$  because the previous probe was not able to detect signals above averaged  $\mu_a = 3 \text{ cm}^{-1}$  over 400-600 nm. In another experiment, a third (S3) and fourth (S4) phantom sets were created with a high range of concentrations (9-33  $\mu\text{M}$ ) of hemoglobin (wavelength averaged  $\mu_a = 2, 3, 4, 5, 6, 7 \text{ cm}^{-1}$ ) and with a fixed low number for scattering in S3 ( $\mu_s' = 10\text{-}12 \text{ cm}^{-1}$ ) and a fixed high number for scattering in S4 ( $\mu_s' = 20\text{-}25 \text{ cm}^{-1}$ ). A summary of the optical properties of all four sets are provided in Table 2.2.

Table 2.2. Average optical properties over 400-600 nm for 4 sets of phantoms (all units in  $\text{cm}^{-1}$ )

Average Optical Properties over 400-600 nm								
Phantoms	S1		S2		S3		S4	
	$\mu_a$	$\mu_s'$	$\mu_a$	$\mu_s'$	$\mu_a$	$\mu_s'$	$\mu_a$	$\mu_s'$
A	0.5	12.6	0.5	22.0	2.0	11.9	2.0	25.3
B	1.1	12.3	1.1	21.5	3.0	11.6	3.0	24.2
C	1.6	12.1	1.6	21.0	4.0	11.2	4.0	23.0
D	2.0	11.9	2.0	20.6	5.0	10.7	5.0	21.9
E	2.5	11.7	2.5	20.2	6.0	10.1	6.0	20.7
F	-	-	-	-	7.0	9.5	7.0	19.6

Prior to making optical measurements, the slit widths of the monochromator were optimized such that the output power from the illuminating fiber is maximized while the full-width at half-maximum (FWHM) of the Xenon lamp spectrum is 4.5 nm in order to resolve the structure of the hemoglobin absorption bands. In the 400-600 nm range, the maximum power was 150  $\mu\text{W}$  at 465 nm, and the minimum power was 50  $\mu\text{W}$  at 600 nm. After a warm up time of 25 minutes, diffuse reflectance spectra were measured over the 400-600 nm wavelength range at increments of 5 nm. The measurements were repeated three times for each phantom. The measurements were made with the room light off and the probe tip in contact with the surface of the liquid phantom. A measurement was also taken from a Spectralon 99% diffuse reflectance standard (SRS-99-010, Labsphere, Inc., North Sutton, NH) with the probe tip in contact with the puck at the end of each phantom study. This spectrum was used to correct for the wavelength-dependent response of the system and throughput of the instrument. For the darkest, most absorbing phantom measured in these experiments, the calculated average signal to noise ratio (SNR) over all wavelengths was  $60 \pm 10 \text{ dB}$ , with a minimum SNR of 41 dB at 400 nm and a maximum SNR of 84 dB at 480 nm, where  $\text{SNR}_\lambda = 20 \cdot \log(I_{\text{avg},\lambda}/\sigma_\lambda)$  where  $I$  is the intensity and  $\sigma$  is the standard deviation at the intensity. This is an improvement compared to probe P3-2 designed and tested in year 2. P3-2 had an average SNR of 42.9 dB, and a minimum SNR of 24.6 dB at 410 nm. Furthermore, it is important to note that the darkest phantom used for the P3-2 experiment was actually much lighter than the one used in the new probe. For comparison, a phantom from this experiment that had comparable optical properties as the darkest phantom in the P3-2 experiment was Phantom S1-D, which had an average SNR of 65 dB over 400-600 nm, and a minimum SNR of 51 dB at 400 nm. This was not unexpected because we had designed the new probe to have a larger collection area and shorter source-detector separation to have higher throughput and collection efficiency.

All 4 sets of phantoms from the 2 different experiments (S1+S2 and S3+S4) were used in the Monte Carlo inversion to extract optical properties. Figure 2.4 shows the extraction performance using the modified system along side the original bench-top system. The absorption and reduced scattering coefficients at each wavelength for each target phantom were averaged over all reference phantoms and presented in the extraction plots. For the modified system with the newly designed probe, the correlation coefficients for expected and extracted  $\mu_a$  and  $\mu_s'$  are 0.9992 and 0.9078, respectively. The overall  $\mu_a$  error was  $8.6 \pm 11.2\%$ , and the overall  $\mu_s'$  error was  $15.6 \pm 14.5\%$ .

For this similarly wide range of optical properties, the original benchtop system had overall errors of  $24.6 \pm 45.2\%$  and  $8.6 \pm 4.0\%$  for  $\mu_a$  and  $\mu_s'$ , respectively. Monte Carlo inversions were also performed separately for the two different days of phantom studies. Extractions with only S1 and S2 combined resulted in  $\mu_a$  and  $\mu_s'$  errors of  $7.5 \pm 7.2\%$  and  $5.5 \pm 5.0\%$ , respectively. This is an improvement from the initial probe geometry of P3-2 presented in year 2. Extractions from the second phantom experiment with only S3 and S4 combined resulted in  $\mu_a$  and  $\mu_s'$  errors of only  $5.3 \pm 4.4\%$  and  $11.7 \pm 11.2\%$ , respectively. This is a very similar phenomenon found in a comprehensive phantom study using our original bench-top system. We found that the extraction accuracy improves when the range of optical properties of reference and target phantoms is narrowed. Although our extracted reduced scattering coefficient errors are nearly doubled that of the original bench-top system, the fact that our absorption coefficient extraction errors are nearly 3 times less than that of the bench-top system for such a wide range of optical properties is a vast improvement from the previous design in year 2.

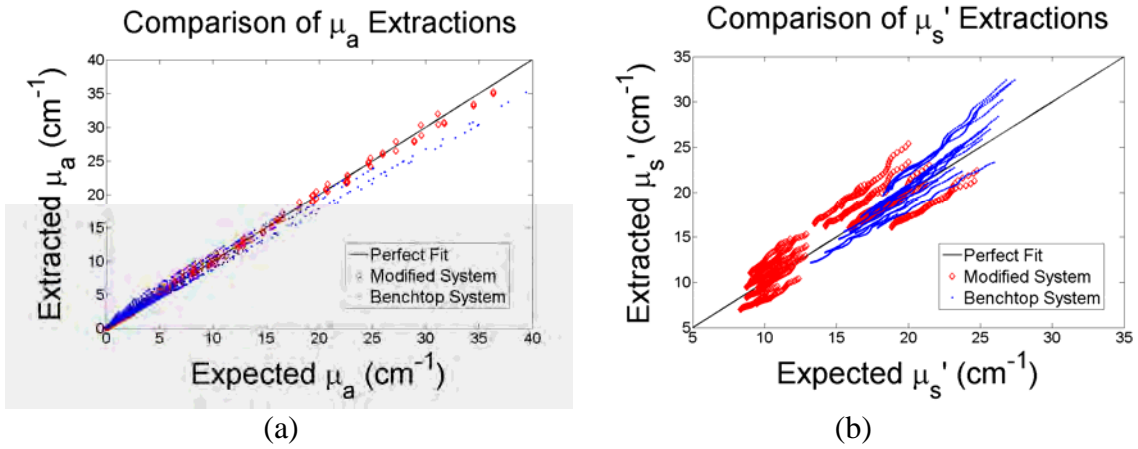


Figure 2.4. Comparison of (a)  $\mu_a$  and (b)  $\mu_s'$  extractions by both systems.

#### D. Wavelength reduction of phantom data

To further miniaturize the system and reduce the cost in the future, we also investigated the potential of replacing the Xenon lamp and monochromator by using several inexpensive LEDs in the 400-600 nm range. We performed simulations of wavelength reduction on the measured liquid phantom data previously obtained with our modified single-pixel probe. Five commercially available LED wavelengths in the 400-600 nm spectral range were chosen: 405, 450, 470, 530, and 590 nm.

The key assumption in the simulation was that each wavelength has a bandwidth of 20 nm with a Gaussian distribution. This was an approximation made based on the commercially available LED specifications. The collected spectra from the phantom studies were processed such that data points from all wavelengths were excluded, except for those of the LED wavelengths enumerated previously. Each phantom spectrum was first convolved with each of the Gaussian-distributed LED emission spectrum, and then integrated over  $\pm 50$  nm from the center wavelength of the LED. This generated 5 individual data points which are assembled into a new spectrum to be fed into the inverse MC model to extract optical properties. Figure 2.5 shows the measured spectra of the lowest and highest absorbing phantoms for all wavelengths and the generated data points from the wavelength reduction simulation used for additional MC inversions, both calibrated by the puck spectrum.

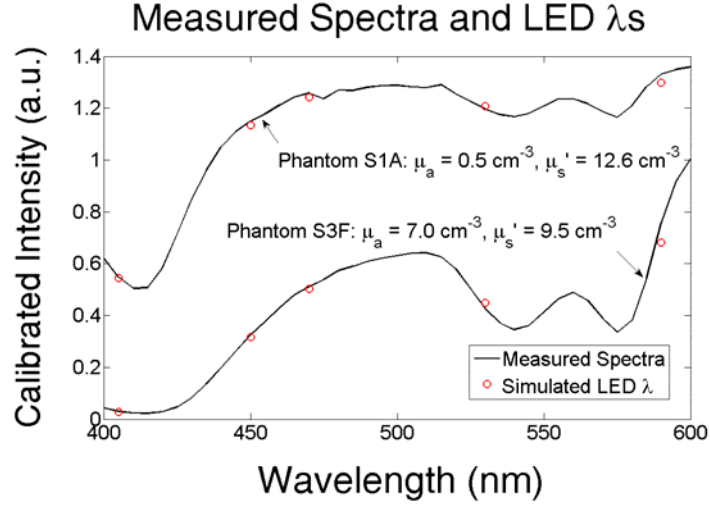


Figure 2.5. Experimental spectra from lightest and darkest phantoms with the 5 wavelengths chosen to for MC inversions

Figure 2.6 shows the extraction performance of the new single-pixel probe after wavelength reduction simulations. For the same large range of optical properties, the overall  $\mu_a$  extraction error was  $10.9 \pm 11.2\%$ , and the overall  $\mu_s'$  error was  $23.9 \pm 26.7\%$ . The correlation coefficients for expected and extracted  $\mu_a$  and  $\mu_s'$  are 0.9972 and 0.8328 in the inversion of wavelength-reduced phantom data. Similar to the inversion from the full spectrum of experimental data, these are the results over a very wide range of optical properties and with data collected from two different days. When the data are broken down into two separate inversions for the two different days, the optical property range is narrowed, and the errors are reduced considerably. The extracted errors from wavelength-reduced S1 and S2 were  $7.2 \pm 6.6\%$  and  $7.4 \pm 6.3$  for  $\mu_a$  and  $\mu_s'$ , respectively. For the highly absorbing phantom sets, S3 and S4 combined, the error was  $7.3 \pm 5.5\%$  for  $\mu_a$  and  $17.6 \pm 20.3\%$  for  $\mu_s'$ .

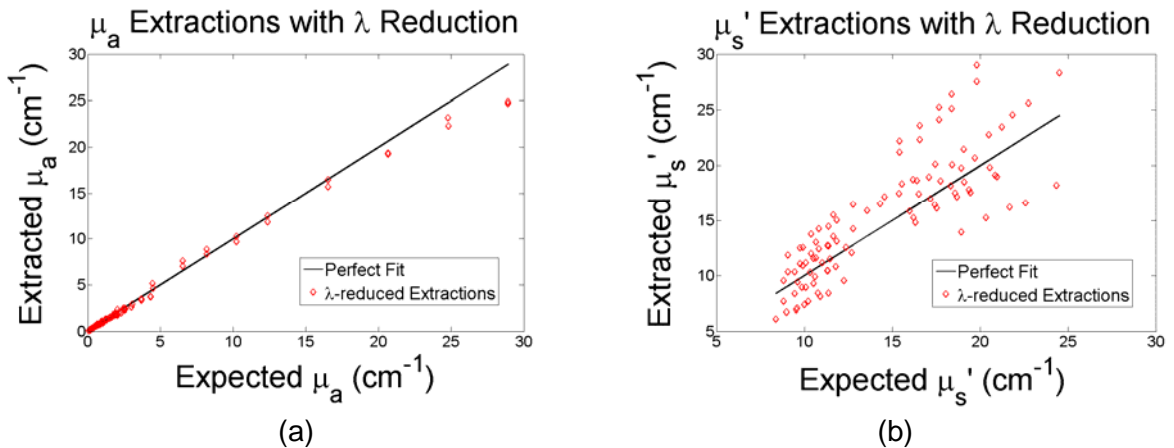


Figure 2.6. Extractions of (a)  $\mu_a$  and (b)  $\mu_s'$  after wavelength reduction simulation

Using only 5 wavelengths from the collected phantom data to perform the Monte Carlo inversion, the hemoglobin spectra can also be reconstructed with the extracted absorption coefficients and the molar extinction coefficient for hemoglobin. Figure 2.7(a) shows the reconstructed hemoglobin spectra averaged over all phantoms. Figure 2.7(b) shows relatively good extraction accuracy for

hemoglobin concentrations for all phantoms. There is a slight underestimation of hemoglobin at very high concentrations, which is also consistent with previous studies using our original bench-top system.

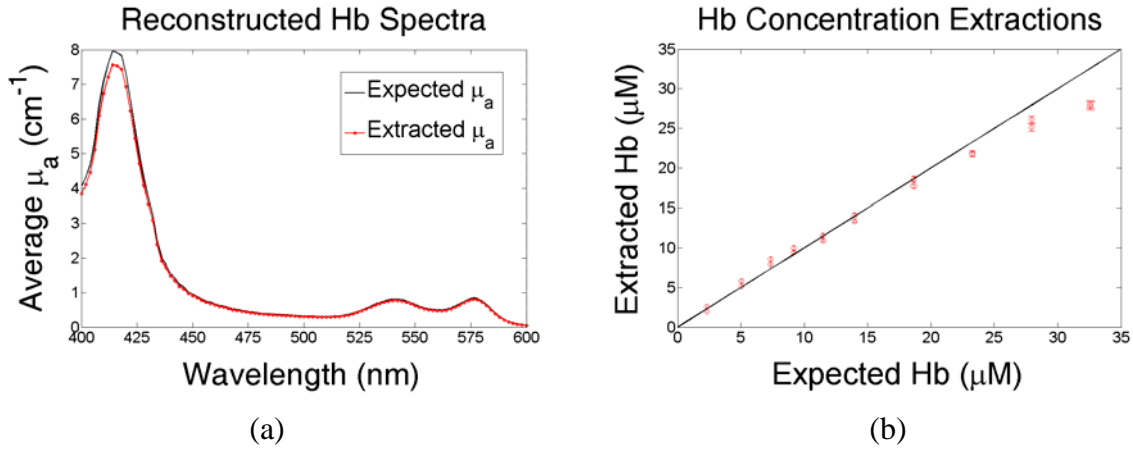


Figure 2.7. (a) Reconstructed Hb spectra averaged over all phantoms using extracted  $\mu_a$  values at the chosen wavelengths; (b) Extractions of Hb concentration by inverting wavelength-reduced data.

These wavelength reduction results show the feasibility of replacing the Xenon Arc lamp, the monochromator, and the illumination fiber in our modified system with just 5 LEDs in the next generation of system design to be described later in this progress report. Not only is there an abundance of high-powered LEDs in the 400-600 nm range, these potential light sources are also very inexpensive. The next generation LED-photodiode device would have the benefits of having the superior quantum efficiency of the detector, but also much higher throughput with LEDs, which can generate up to more than 1 W of power.

### E. Multi-pixel probe design and fabrication

A primary goal in the future iterations of device design involves multiplexing the single-pixel into a quantitative spectral imaging device. This can be done by arranging multiple optical fiber-photodiode pairs in a matrix formation. An important new parameter that must be characterized is the crosstalk. While ideally each fiber-photodiode pair should be treated as a single pixel, the issue of a detector collecting stray light from an adjacent pixel(s) is unavoidable. High levels of crosstalk can significantly affect the measurement accuracy from tissue directly below the pixel.

The first step in analyzing cross talk was to simulate a simple case where two single-pixels are placed next to each other. The geometry was determined by placing the two pixels as physically close as possible, with the edges of the detectors flush against each other. This yielded a separation distance of 8 mm between the two illumination fibers. A Monte Carlo forward model of reflectance was used to estimate the signal (from central fiber) and cross-talk (from adjacent fiber) for one of the pixels. Measurements were also taken experimentally to compare the forward modeled spectra to actual data. Hemoglobin was used as the absorber and polystyrene spheres were the scatterers. The optical properties used in both the forward model and measured data were  $\mu_a = 0.25 \text{ cm}^{-1}$  and  $\mu_s' = 10 \text{ cm}^{-1}$  (average values over 400-600 nm)

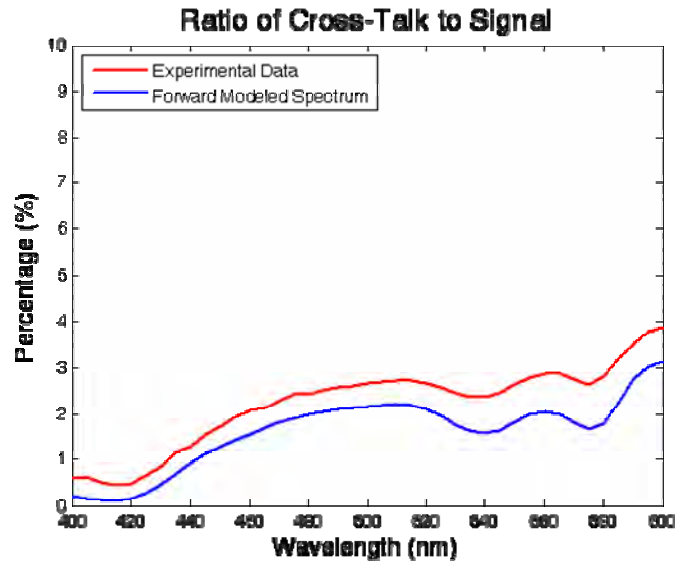


Figure 2.8. Comparison between experimentally measured cross-talk and forward modeled cross talk. The results indicate that the actual cross talk is close to the model expectations.

The comparison of these two spectra, shown in Figure 2.8, indicates that the forward model and experimental data of cross talk are in fairly good agreement, with both indicating the cross talk levels would be <5%.

While providing a starting point, a two pixel system is too inadequate to be classified as an imaging device. We propose a slightly more complex design suitable for use as an imaging device. The two-pixel design was further multiplexed to create a nine pixel system arranged in a 3x3 matrix formation depicted conceptually in Figure 2.9.

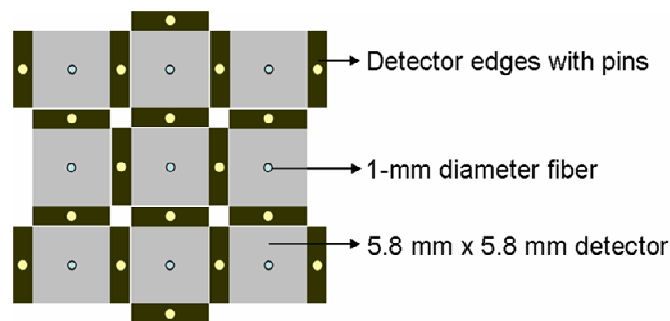


Figure 2.9. A 3x3 imaging matrix used for simulating crosstalk. Cross talk is more of a concern in this design, with each pixel receiving cross-talk from multiple sources.

The forward model was used again to generate the diffuse reflectance spectrum including both signal and cross-talk (from all adjacent sources) for each pixel based on the matrix geometry. As expected, each pixel would detect more cross talk than the simple two-pixel case due to the increase in adjacent pixels. In addition, the cross talk would vary based on the pixel position. Notably, the central pixel in the 3x3 matrix, shown previously in Figure 2.9, would detect the most cross talk, the side pixels would detect the second most cross talk, and the corner pixels would detect the least amount of cross talk.

Because looking directly at the crosstalk does not provide meaningful information about the

efficacy of the probe, we investigated the effect of crosstalk on the model's accuracy of extracting optical properties. Spectra were simulated for five phantoms with a wide range of average absorption coefficients over 400-600 nm ( $\mu_a = 0.4, 0.9, 1.3, 1.6, 2.0 \text{ cm}^{-1}$ ) and a fixed reduced scattering coefficient ( $\mu_s' = 10 \text{ cm}^{-1}$ ). The simulated spectrum from each pixel was then inverted to determine the effect of cross-talk on the extracted optical properties. The inversion assumes each pixel is independent thus only includes the central illumination fiber, while forward modeled data includes both the signal (central illumination) and all cross-talk (adjacent illumination fibers). Because the same model was used for both the forward model and inversions any errors in the inversion are solely contributed to the cross-talk.

Table 2.3 enumerates the inversion errors in the presence of crosstalk at the center, the side, and the corner detectors, respectively. The errors were averaged over all reference-target phantom combinations. As expected, the inversion showed that center detector had the worst extraction errors for  $\mu_a$  and  $\mu_s'$ , approximately doubling the errors from those of the side and corner detectors. With  $\mu_a$  and  $\mu_s'$  extraction errors of less than 2% and 5%, respectively, crosstalk has little effect on the side and corner detectors. Although the center detector received the most crosstalk, the extraction errors are still less than 5% for  $\mu_a$  and 10% for  $\mu_s'$ . These results indicate that the overall errors due to crosstalk are relatively small and that constructing an imaging device will be feasible based on this particular geometry.

Table 2.3 The  $\mu_a$  and  $\mu_s'$  extraction errors (%) for each detector in the presence of crosstalk in phantoms ranging from low to high absorption coefficients ( $\mu_a = 0.4 - 2.0 \text{ cm}^{-1}$ ) and medium reduced scattering coefficients ( $\mu_s' = 10 \text{ cm}^{-1}$ ), averaged for all reference-target phantom combinations.

Inversion errors with crosstalk						
Phantoms	Center Detector		Side Detectors		Corner Detectors	
	$\mu_a$ error	$\mu_s'$ error	$\mu_a$ error	$\mu_s'$ error	$\mu_a$ error	$\mu_s'$ error
A	2.2	7.8	1.6	5.7	1.0	2.9
B	2.2	5.1	1.6	3.6	0.9	1.8
C	2.4	5.0	1.6	3.3	0.9	1.8
D	3.6	6.5	1.8	3.8	1.3	2.3
E	4.3	8.1	2.4	4.8	1.7	3.1

The promising results of these simulations prompted us to move forward with fabrication of the imaging probe. The same type of optical fiber and photodiodes used for the single pixel device P4-3 were used to construct the 3x3 matrix imaging probe (Figure 2.10). The nine detectors were fixed on a PCB board and holes for the optical fibers were drilled through the center of each detector. With construction of the imaging probe complete, experiments are underway to evaluate the feasibility of this quantitative imaging probe.



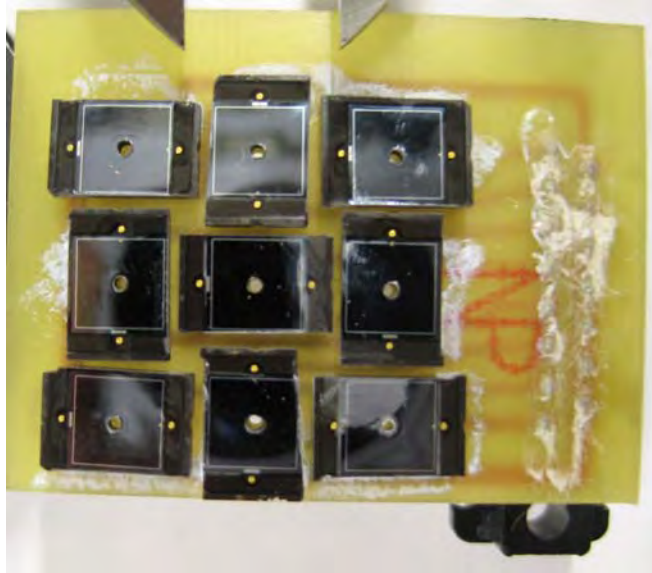


Figure 2.10. Photograph of the 3x3 imaging array.

An important modification to a system component was required in order to read and collect data from the 3x3 imaging probe. With the single pixel device a single-channel current amplifier (Terahertz Technologies, PDA-750) could easily read and collect the photocurrent. However, the same current amplifier could not be used to efficiently collect data from the 3x3 imaging probe. Therefore we needed to design and construct a multi-channel current amplifier, capable of simultaneously reading the photocurrent from all nine photodiodes. We chose to use five commercially available dual-channel transimpedance amplifier circuit boards (Boston Electronics, TWAMP). Preliminary results with the imaging probe indicated the detected photocurrent was on the order of 1 to 10  $\mu\text{A}$ . The  $10^7$  gain on the circuit boards were sufficient to boost our signals to a measurable level. The circuit boards were properly wired and shielded inside an aluminum enclosure.

A data acquisition card (NI, USB-6210) was used to digitize the output voltage signals from the amplifiers and send the measurements to a computer running a LabView-based interface. Using 10 analog input channels on the DAQ card, each channel was capable of a 25 kS/s sampling rate, more than sufficient for reading the output voltage of the amplifiers. The completed device was a fully functional 10-channel current amplifier which easily interfaced with both the 3x3 imaging probe and computer (depicted in Figure 2.11).

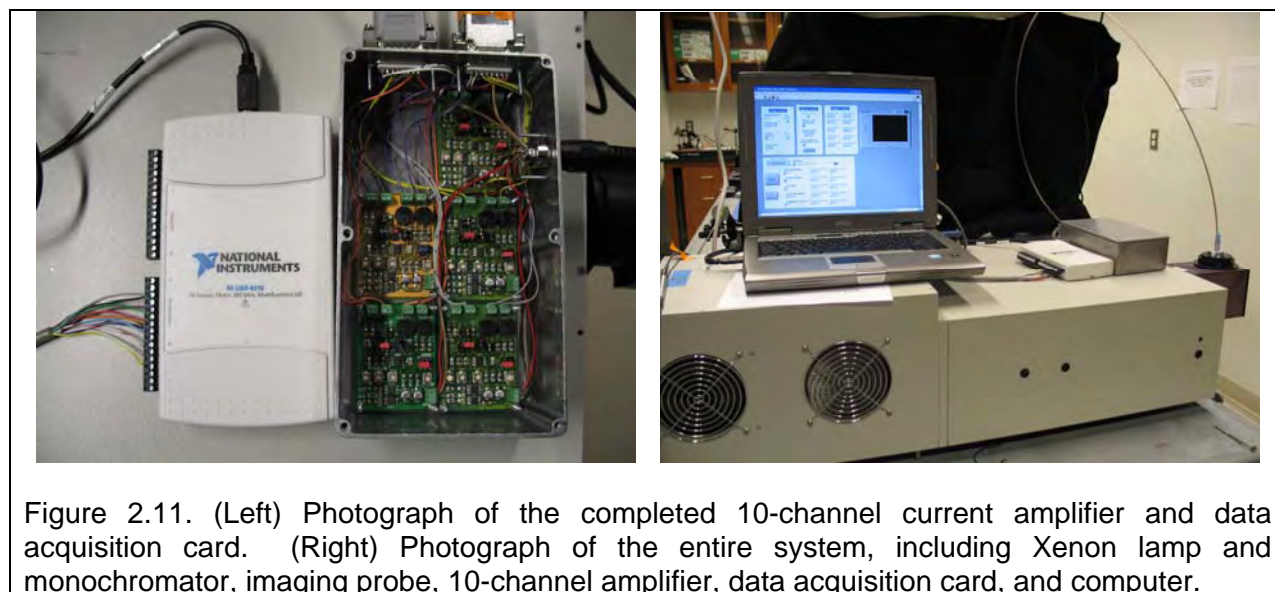


Figure 2.11. (Left) Photograph of the completed 10-channel current amplifier and data acquisition card. (Right) Photograph of the entire system, including Xenon lamp and monochromator, imaging probe, 10-channel amplifier, data acquisition card, and computer.

### Plans for years 4 and 5

Due to the deviation of the SOW for years 1-3, our research plans on the system-on-a-chip for years 4 and 5 are also revised accordingly.

#### Year 4:

- To complete the construction of the 3x3 multi-pixel system and test it in liquid tissue phantoms.
- To investigate a new xenon light source with a filter wheel for better light coupling between the lamp and the fibers and reduced number of wavelengths in phantom studies.
- To replace the silicon detector with a GaAs detector plate which has improved sensitivity and can be customized for our specific illumination and collection geometry.
- To assemble a first prototype back-illuminated spectral imaging device and construct the electronics box.

#### Year 5:

- To use the multi-pixel fiber-photodiode device to collect spectra from 5 – 10 ex-vivo lumpectomy specimens.
- To analyze the spectra data collected using the fiber-photodiode device and the BISI device.



### 3.1 Project 2: Exploiting, physiological, metabolic and molecular contrast in breast cancer

#### A. Original SOW for five years

- 1) *Physiological and metabolic characterization of mammary tumors in an animal model of breast cancer.* Nude mice will be injected in the flank with 500,000 4T1/D2 cancer cells. The tumors will be allowed to grow until they have reached a size of approximately 8 mm in diameter (approximately 1-2 weeks). Non-invasive optical measurements of tumor oxygenation, vascularity and metabolism will be measured using a continuous wave system and compared to independent measurements of tumor hypoxia using an OxyLite fiber optic sensor and immunohistochemistry of hypoxic and metabolic markers (year 1).
- 2) *Synthesis of contrast agents for molecular imaging.* Gold nanoparticles will be prepared via citrate reduction of chloroauric acid. The particle size will be adjusted to preferentially scatter NIR light. Anti-HER2 and anti-EGFR antibodies will be conjugated to the gold. The scattering spectrum of (1) the pre-labeled nanoparticles will be measured to verify their NIR resonant scattering properties and (2) the labeled nanoparticles to verify binding with the antibodies (a characteristic red-shift in the peak is expected to occur after binding) (year 2).
- 3) *Molecular imaging in cells.* Human breast cancer cell lines, MDA-MB-468 and SK-BR-3 which over express EGFR and HER2, respectively will be cultured to test the targeting strategies. Cell lines that express low levels of EGFR and HER2 will be used as controls. Each cell type will be labeled according to previously established protocols and imaged using a microscope coupled to a CCD camera. The optical contrast in the cells over expressing HER2 and EGFR receptors relative to that in the control cells will be statistically compared to demonstrate the molecular specificity of the anti-EGFR and anti-HER2 nanoparticles (year 3).
- 4) *Molecular imaging in animal models.* Tumor cell lines will be stably transfected to over express both HER2 and EGFR, and tumors will be grown in the mammary fat pad of the nude mice used in (a). Both topical and systemic injection of the molecular contrast agents will be explored. An optical imaging system consisting of a tunable laser and a CCD camera will be used to image the molecularly tagged contrast agents for different doses (to measure the effect of dosimetry on the signal to background) as well as for topical vs. systemic delivery. Note that task (a) is directly relevant to this aim as it will provide the instrumentation and algorithms for data analysis as well as experience with the preparation of animal tumor models for these studies (years 4-5).

The original project proposed here has evolved into two distinct projects: (1) The development of techniques to exploit the intrinsic sources of optical contrast (physiologic and morphological) as a means to assess response to cancer therapy and (2) the assessment of extrinsic sources of optical contrast for use as an aid in intra-operative assessment of breast tumor margins.

#### B. Summary of Accomplishments in year 1

The goal of this year 1 study was to quantify and track changes in oxygenation in response to carbogen breathing in 4T1 breast tumors in nude mice using optical spectroscopy. Specifically we measured hemoglobin saturation and the optical redox ratio and compared the optical measures of oxygenation to that of a well established method of measuring tumor  $pO_2$ , the OxyLite system, to demonstrate the utility of optical spectroscopy to quantitatively monitor tumor physiology in a pre-clinical model. Non-invasive optical spectroscopy was performed on 4T1 breast tumors grown in the flank of nude mice ( $n=10$ ) before and after the administration of carbogen (95%  $O_2$ , 5%  $CO_2$ ), by placing a fiber optic probe in contact with the surface of the tumor.

This work established the ability of optical spectroscopy to consistently track changes in tumor physiology in response to a perturbation. It was found that optical spectroscopy may in fact provide a more robust assessment of tissue oxygenation than the existing Oxylite system, likely due to its larger probing volume. This work establishes optical spectroscopy as a viable tool to monitor changes in tumor physiology in response to other treatments, including radiation, chemotherapy, and molecular therapies, offering many advantages over existing technologies. In particular, it is fast, non-invasive, quantitative, and probes a wide range of physiologic parameters, including blood content, oxygenation, and cellular metabolism. This project has subsequently expanded and will span the full five years of the proposal.

### **C. Summary of Accomplishments in year 2**

The research goals for year 2 have changed from the synthesis of scattering contrast agents that was originally proposed to detecting mammary cancer with fluorescent contrast agents. Fluorescence agents were chosen over scattering contrast agents because fluorescence has a unique excitation and emission. In the previous year, aminolevulinic acid (ALA) induced protoporphyrin IX (PpIX) was successfully used to differentiate cancerous cells from normal with fluorescence lifetime. This work was carried on into the beginning of this year by examining fluorescence intensity and spectroscopy. It was found that PpIX has a significantly greater fluorescence increase in malignant cells as compared to normal cells. However, the raw fluorescence intensity of cells cannot be used to delineate malignant from normal without a fluorescence control to determine the endogenous fluorescence. The long incubation time, 2 hours, and endogenous fluorescence required to detect PpIX is clinically prohibitive. An alternative contrast agent chosen was 2-[*N*-(7-nitrobenz-2-oxa-1,3-diazol-4-yl)amino]-2-deoxy-D-glucose (2-NBDG). We have successfully optimized detection of 2-NBDG and demonstrated that malignant cells have an increased raw fluorescence intensity over normal cells. This is potentially useful for use in margin assessment of mammary tumors.

#### **3.1.1 Predicting the validity of optical biomarkers to quantitatively and longitudinally monitor tumor hypoxia and necrosis in murine tumor models (expansion of accomplishments in year 1)**

Tumor hypoxia is a well known and important factor responsible for the growth and development of tumors and has been known to influence aggressiveness of the tumors, confer increased resistance to treatment and promote metastasis. Given the consequences of tissue hypoxia, determining the oxygenation status of tumors is of paramount importance to determining tumor prognosis and treatment outcome. However, standard methods to measure tumor hypoxia utilize invasive techniques such as using a needle based oxygen electrode or examining biopsied tissues via immunohistochemical assays, or alternately employ expensive imaging modalities such as MRI or PET scanning of the tissues that have previously been treated via exogenous radioactive or heavy-metal based contrast agents. Here we report, for the first time, that using non-invasive optical measurements of diffuse reflectance may provide accurate estimates of tumor hypoxia.

Fifty female nude mice were ordered from the NCI (Bethesda, MD), stored at the Duke animal facility in 12 hours dark/light cycle where were allowed ad libitum and were inoculated subcutaneously with  $10^6$  4T1 mouse breast carcinoma cells suspended in 0.1 ml serum-free medium in their right flank. Once the tumor diameters reached 4-6 mm, the animals were evenly distributed (by tumor volume) into control and treatment groups (each group having 25 animals). The treatment group received a maximum tolerated dose (MTD, 10mg/kg, i.v.) of doxorubicin while the control group received an equivalent volume of saline. The treatment day was labeled day 0. The tumors in both groups were then monitored optically over 2 weeks following the measurement

time-course described below. These animal studies were approved by the Duke Institutional Laboratory Animal Care and Use Committee.

The tumors were monitored optically prior to treatment (day 0) and on days 2, 5, 7, 10 and 13 post doxorubicin or saline administration. The animals were maintained under anesthesia by isoflurane breathing (1.5% Isoflurane gas mixed with oxygen) throughout the course of the optical measurements. Diffuse reflectance spectra were measured between 350-600 nm by pushing the probe to make gentle contact with the tumor surface and held by a clamp at a fixed position throughout the course of the optical measurements. Two measurements of diffuse optical reflectance spectra were collected from each animal at each time-point, consecutively. These measured spectra were analyzed by a previously validated inverse MC model to extract concentrations of HbO<sub>2</sub> (oxygenated hemoglobin) and HHb (deoxygenated hemoglobin) using a previously tabulated database [3]. The inverse MC model fit the measured diffuse reflectance and extracted the concentration of HbO<sub>2</sub>, concentration of HHb, a mean scatterer size and a wavelength-averaged reduced scattering coefficient ( $\langle\mu_s'\rangle$ ) [3]. The averaged values of each of the parameters from the inversions of both measured diffuse reflectance spectra were used as the final estimates for the respective parameters for each tumor.

Five randomly chosen animals, from each group, were removed for immunohistochemical (IHC) analysis on days 0, 5, 10 and 13. These treatment schedules and time-points were selected from pilot studies that showed statistically significant differences in tumor hemoglobin saturation between the treated and control groups. The tumors from the animals designated for IHC were resected, snap-frozen by placing the resected tumor in a container immersed in liquid nitrogen and stored for subsequent histopathological examinations. For each of these animals, the outline of the fiber optic probe was traced on the surface of the tumor immediately after the optical measurement which ensured that the resected tumors could be sectioned parallel to the tip of the fiber optic probe thereby yielding sections from approximately the same tissue volumes as sensed by the optical measurements.

For each tumor, sections were obtained from depths of 600  $\mu$ m and 1.6 mm below the surface. Slides were counted from the start of cutting and numbered consecutively so that the depth of each section from the tumor surface could be estimated. Each section was stained with pimonidazole, Hoechst 33342, and H&E. Pimonidazole as the hypoxia marker was immunostained using a direct labeling protocol. Briefly, tumor sections were fixed in cold acetone for 15 min, blocked in donkey serum blocking reagent. The primary antibody to pimonidazole was first labeled with a fluorescent IgG probe. The sections were then incubated with the labeled pimonidazole antibody for one hour at room temperature, washed with PBS, and fixed with 10% buffered formalin for one minute. Stained tumor sections were kept in 1% formaldehyde phosphate-buffered saline and imaged within 3–4 days. After imaging, sections were stained with hematoxylin and eosin (H&E) to obtain histologic structure and necrotic fraction. To quantify tumor perfusion in these tumors, Hoechst-33342 was injected into each animal via a tail vein right before sacrifice. Hoechst-33342 is a fluorescent dye (excitation wavelength = 340nm, emission wavelength = 450nm) and stains the nuclei of cells around blood vessels, as it passes through the vessel. Thus, vessels with blood flow show perivascular nuclear staining. These tumor sections were examined under a fluorescent microscope which was equipped with an automatic stage and controller with a resolution of 0.025  $\mu$ m per step size was used to scan the entire tumor section to obtain Hoechst stained images. The slides were scanned for Hoechst 33342 fluorescence using a DAPI fluorescence filter to reveal all functional blood vessels, followed by a second scan using TRITC filter on the same slide to identify pimonidazole staining. Images acquired from stage scanning were stitched, overlaid and analyzed.

Microscopic images of the tumor sections were analyzed to measure the hypoxic fractions from pimonidazole staining and necrotic fractions from H&E staining. The hypoxic fraction is defined as

the ratio of hypoxic area versus vital tissue area, across the entire tumor section. The hypoxic area was determined using image thresholding and segmentation on the pimonidazole stained images. Higher intensity level of the fluorescence staining indicated higher hypoxia in the tissue. By thresholding the area with intensity level higher than a given fixed threshold was marked hypoxic

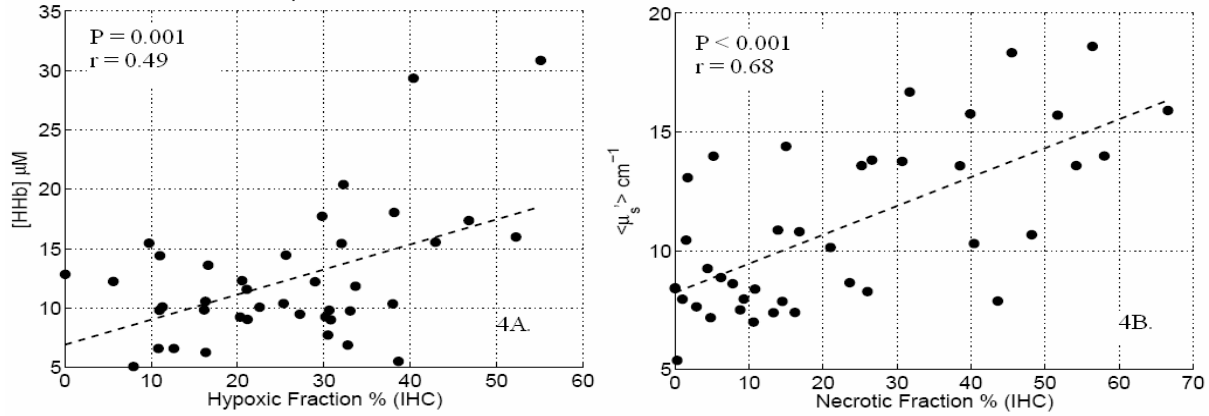


Figure 3.1: Correlations between optical and immunohistochemical endpoints. (Figure 3.1A) shows the correlation between the optically estimated deoxygenated hemoglobin concentration (HHb) and the hypoxic fraction obtained from IHC; (Figure 3.1B) shows the correlation between the wavelength-averaged reduced scattering coefficient and necrotic fractions.

and the hypoxic fraction was calculated using vital tissue with any necrotic areas excluded. Since each tumor had sections from depths of 600  $\mu\text{m}$  and 1.6 mm, the hypoxic fraction for the tumor was taken to be the average value of both sections. The necrotic fraction was measured based on the H&E staining. The necrotic area was characterized by higher Eosin staining, dark and condensed nuclei debris, and incomplete cell shapes. The necrotic fraction was calculated by the ratio of the necrotic area to the overall vital tissue area across each section. As before, since there were two sections corresponding to two depths for each tumor, the averaged values were considered as the necrotic fraction for the tumor.

The optical estimates of HHb and  $\langle\mu_s'\rangle$  were compared to the IHC estimates of hypoxic fraction and necrotic fraction, in a pair-wise manner. Correlations were determined via the Pearson's liner rank coefficient and were considered significant for  $P < 0.05$ . Statistical correlations between the optical parameters extracted from the inverse Monte Carlo model and the IHC variables extracted from histology were evaluated. Figure 1 shows correlations between the optically extracted values of tumor HHb concentration and  $\langle\mu_s'\rangle$  with the immunohistochemical estimates of hypoxic fraction and necrotic fractions, respectively, in a total of 40 animals. As seen in Figure 3.1A the HHb concentration was positively correlated with hypoxic fraction, while Figure 3.1B shows that the wavelength-averaged reduced scattering coefficients were positively correlated with histologically assessed necrotic fractions. It should be noted that the optical and immunohistochemical variables constituted paired measurements on individual animals at distinct time-points. The positive correlation between the HHb and hypoxic fraction can be interpreted in a straightforward manner, i.e., increased tumor hypoxia leads to higher levels of increased HHb concentration. The strong correlations between the necrotic fraction and the extracted mean reduced scattering coefficients indicates that this optical parameter provides a sensitive means to quantify changes in tissue structure caused from necrotic tissue damage. We surmise that the increase in tissue scattering coefficient arises from the increased fluctuations in the refractive index within the tumor, which are a result of necrotic tissue damage. Given these results, we infer that the estimated values of HHb concentration and mean reduced scattering coefficient from the diffuse reflectance spectra provide optical analogues of tissue hypoxia and necrosis, respectively.

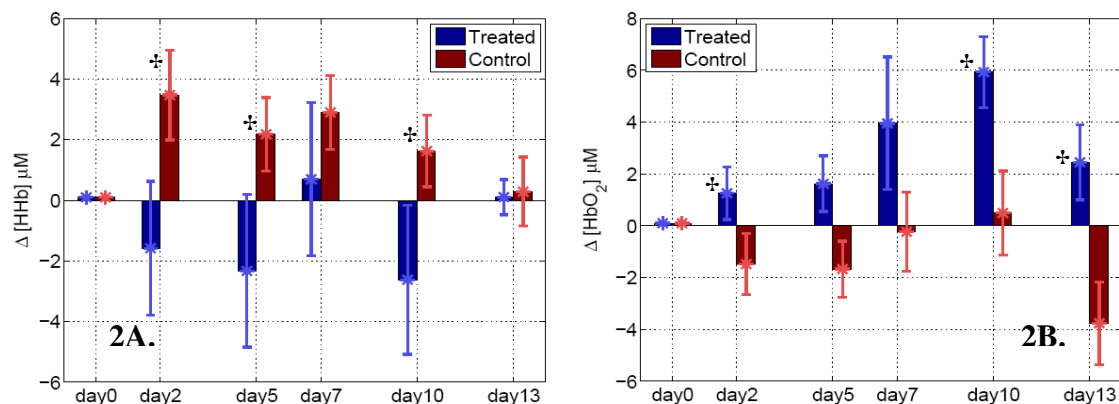


Figure 3.2: Longitudinal changes in mean, baseline-normalized HHb concentrations (Figure 3.2A) and mean baseline-normalized HbO<sub>2</sub> concentrations (Figure 3.2B) for the treated and control tumors. The bars represent the mean values averaged across all animals within a group for each time point, while the dagger symbols indicates the time-points when the groups differed significantly from each other. The error bars represent the standard error.

Figures 3.2A and 3.2B show the longitudinal changes in mean, baseline-normalized HHb concentrations (Figure 3.2A) and mean baseline-normalized HbO<sub>2</sub> concentration (Figure 3.2B) for the treated (blue bars) and control (red bars) tumors. Here, the baseline normalized values for each animal were calculated as the difference between the value of the optical parameter at each time-point and its value measured on day 0. To distinguish this baseline normalized value from the measured raw value of the parameter, it is indicated by a  $\Delta$ -prefix next to the variable. Each bar represents the average value of the baseline normalized optical variable averaged across all animals in each group, at each given time point. These data demonstrate a unique feature of the optical measurements – the capability to serially, repeatedly and non-destructively follow tumor physiology in the same animal across time. It is seen from the data shown in Fig 2A that average HHb concentrations in the treated animals remained lower than the control group throughout the course of measurements indicating that the tumors in the control animals remained relatively more hypoxic than the treated animals. The trends in the baseline normalized HbO<sub>2</sub> values in Fig 2B show that the tumor oxygenation in the treated animals was higher than those in the control animals throughout the course of the experiments. Comparisons between the treated and control groups on each day showed that they showed statistically significant differences ( $p < 0.05$ ) in the baseline normalized HHb values on days 2, 5 and 10, and in the baseline normalized HbO<sub>2</sub> values on days 2, 10 and 13 (indicated by the daggers in Figure 3.2A and 3.2B).

This work has been submitted for publication to Cancer Research and is currently under review.

#### Plans for year 4

For the next year, we plan to investigate whether optical spectroscopy can successfully predict response to radiation treatment administered to murine models of cancer. For this study, we will inoculate 50 nude mice with human pharyngeal squamous cell carcinoma (FaDu) in the flank. We plan to use this cell line because the efficacy of radiotherapy on this cell line in nude mice models has been extensively studied and reported [4-7]. Once the tumor volumes reach 150-300 mm<sup>3</sup>, we will randomize the animals into a control and treated group. The tumor bearing flanks of the animals in the treated group will receive a previously calculated TCD50 dosage of 38 Gy that will be delivered locally to the animals [8]. The local dosage will be ensured by anesthetizing the animals via Nembutal and extending their legs into the field of radiation, while shielding the rest of their bodies using a custom built lead radiation shield. The control animals will undergo sham

irradiation following the same protocol. We will obtain optical spectroscopic measurements one day prior to treatment (for baseline values) and then each day post irradiation for the first 7 days, and then, subsequently, every other day for the next two weeks from all animals undergoing the study. The tumor volumes of the animals will be measured Monday and Friday of every week until 120 days post treatments, or until the tumor burdens become too large to bear.

We will assess changes in the optical estimates of changes in HbO<sub>2</sub>, HHb and total Hb concentrations (relative to each animal's baseline values) between the treated and control animals across each day of the optical measurements. Next, for all the animals belonging to the treatment cohort, we will examine the hazard ratios using Kaplan-Meier log-rank survival curves to determine if there are any significant differences in the survival ratios when the animals were classified according to a binary decision criterion using each of the most significant biomarker that showed maximal differences between the treated and control cohorts, at each time-point. This will allow us to examine the predictive value of each available optical biomarker in determining the outcome of treatment. We expect that to find at least one parameter over the course of the first 3 weeks post treatment to provide predictive ability to distinguish animals that showed complete response vs. partial response to the treatment.

### **Plans for year 5**

In Year 5, we will employ core-needle optical spectroscopy clinically to evaluate A) whether pre-therapy optical biomarkers are prognostic, or predictive for response to neo-adjuvant chemotherapies, and B) whether these optical biomarkers may be useful for monitoring tumor response to therapy. We have previously conducted a clinical study of our technology on 40 patients, in which an optical probe was inserted into normal and malignant tissues *in vivo* during breast cancer surgery. We found that malignant tissues exhibited significantly lower overall hemoglobin saturation than normal tissues. However, we also discovered that while a number of malignant tissues were severely or moderately hypoxic, a significant number were also normoxic, indicating that not all tumors exhibit hypoxia. Closer examination revealed that the normoxic tumors were correlated with HER2/neu gene amplification and higher hemoglobin content. This is consistent with a model of increased tumor oxygenation created by enhanced tumor perfusion, which is a result of increased angiogenesis promoted by the HER2/neu gene. Tumor hypoxia is an important prognostic factor in breast cancer, and may also be predictive for response to tumor therapy (both radiotherapy and chemotherapy). However, there are currently no satisfactory methods with which to measure hypoxia *in vivo*, prior to removal of the tissue.

Therefore, in Year 5, we propose a clinical study to measure the pre-therapy and post-therapy oxygenation levels in breast cancer patients undergoing neo-adjuvant chemotherapy. Prior to commencement of chemotherapy, we will insert our optical probe (through a biopsy cannula) into the tumor, and optical biomarkers (including total hemoglobin content, hemoglobin saturation, and beta carotene concentration) will be measured. These measurements will serve as a baseline for further comparison. After completion of therapy, we will again measure the optical biomarkers of the remaining tumor *in vivo* (this will be done during surgery to remove the patient's tumor, but the measurement methodology will remain the same). Clinical and pathologic markers of tumor response to therapy (i.e. the RECIST criteria and pathologic assessment) will be recorded to determine the extent to which the patient responded to the particular therapy. We will compare pre- and post-therapy optical biomarker measurements, and correlate the changes with clinical treatment response criteria. We will also establish correlations between pre-therapy optical biomarker levels and clinical treatment response criteria. By determining how optical biomarkers change over the course over treatment, we may identify which biomarkers may be useful for serial monitoring of response to tumor therapy. In addition, by establishing a correlation between pre-therapy optical biomarker levels and ultimate clinical and pathological tumor response criteria, we can perhaps identify particular biomarkers which could predict for response to certain therapies

before the therapy is prescribed, which would be another important step toward personalized oncology.

### **3.1.2 ALA as a Contrast Agent (expansion of accomplishments in year 2)**

Fluorescence lifetime was analyzed in the previous year. However, fluorescence lifetime can be difficult to discriminate if a large number of fluorophores are present, is computationally intensive and may require long imaging times (60 seconds integration time). Therefore, intensity images and spectroscopy data were obtained. Also, the mammary cell lines tested were changed and expanded from the previous year to include negative and positive estrogen receptor (ER-/ER+, respectively) cell lines.

#### **A. Cell Study Design**

Six mammary cell lines were chosen for intensity imaging and spectroscopy:

- MCF10A - Normal
- Human mammary epithelial cells (HMEC) - Normal
- MDA-MB-231 - Malignant ER-
- MDA-MB-435 – Malignant ER-
- MCF7 – Malignant ER+
- MDA-MB-361 - Malignant ER+

Cell lines were treated with 500 µg/mL ALA dissolved in cell media or cell media alone and allowed to incubate for 2 hours and then imaged. This concentration was determined from previous literature, and the time was determined as optimal after the kinetics over 6 hours was observed (data not shown).

Cells were imaged with spectral confocal fluorescence microscopy at an excitation of 405 nm. Six experimental and six control cell dishes with 2 images per plate per cell line were analyzed after ALA addition (500 mg/mL in fresh cell media) or fresh media alone 2 hours prior. Fluorescence intensity was captured at a bandwidth between 610-700 nm. Fluorescence spectroscopy measurements were completed from 420-750 nm with a bandwidth of 20 nm and stepsize of 10 nm to meet the Nyquist theory and not photobleach the cells.

Fluorescence intensity analysis of control and treated cells was completed by manual discrimination of individual cells with background subtraction. Cell intensities were averaged per image (N=12, control and treated). Fluorescence intensity was calculated as a percent change in cellular fluorescence between control and treated.

#### **B. PpIX Fluorescence Intensity**

Figure 3.3 shows representative images of treated and untreated normal and malignant cells with different receptor status after 2 hours. This figure qualitatively shows the normal cells have a bright untreated intensity per cell and the malignant become much brighter with treatment. The high baseline signal in the normal cells is due to excitation of FAD at 405 nm (as verified with spectroscopy).

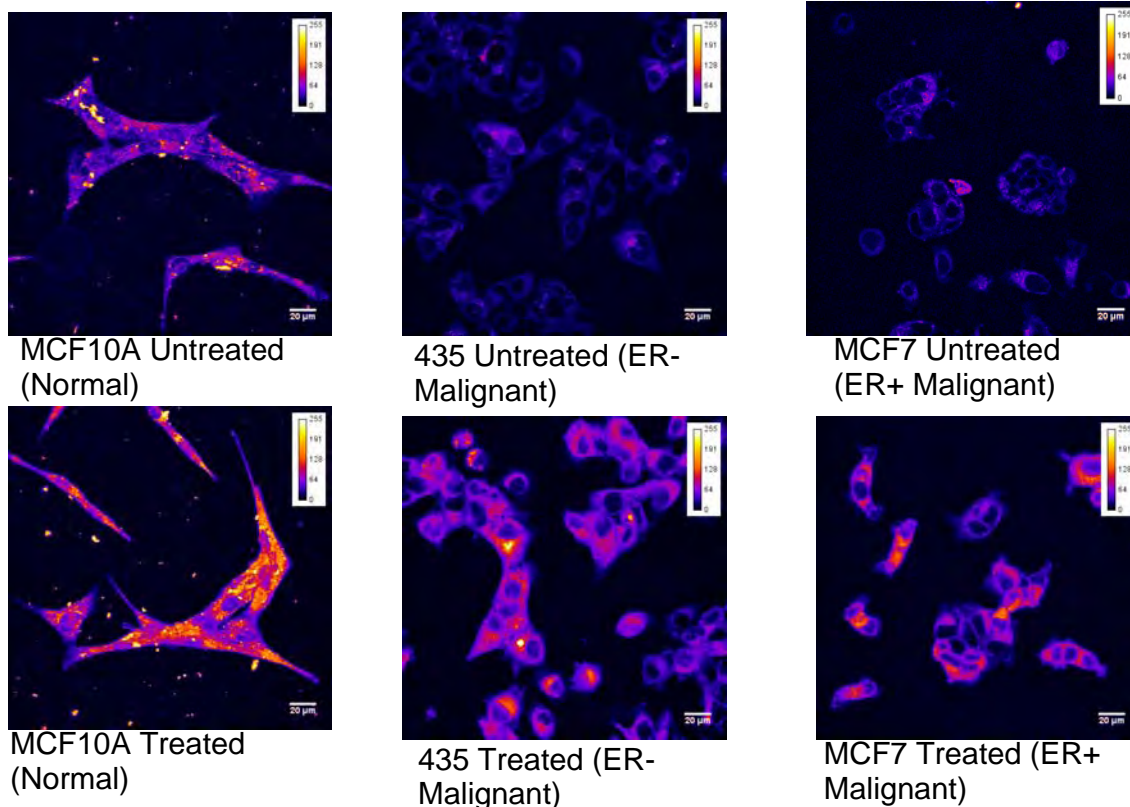


Figure 3.3. Representative confocal fluorescence images of normal and cancer cells treated with ALA for 2 hours. Excitation was at 405 nm and emission was collected between 610-700 nm.

Mean fluorescence intensity for all six cell lines is shown quantitatively in Figure 3.4. The error bars represent the standard deviation. Wilcoxon Rank Sum tests were completed for statistical comparisons and all ALA treated cells are significantly greater than the untreated cells. However, comparing treated malignant cell mean fluorescence to treated normal cells do not show significant differences. This is due to the contribution of endogenous FAD fluorescence in the normal cells in the 610-700 nm. Our results show that within breast cancer cells the raw fluorescence intensity of PpIX can vary with the administration of the same concentration of ALA. These results are similar to those found previously in literature where various organ systems were examined and large differences were found in PpIX production[9].



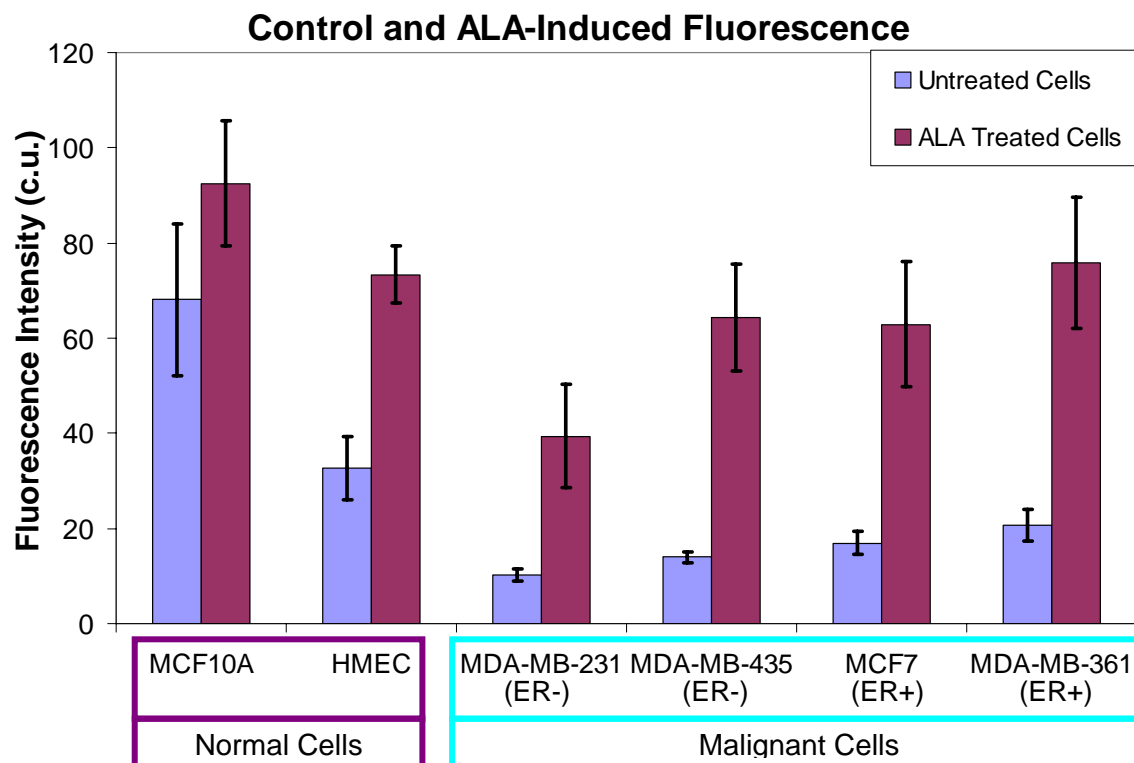


Figure 3.4: Average and standard deviation of the fluorescence intensity in each image. Fluorescence was obtained from 610 – 700 nm and values were obtained by raw intensity value - background. All ALA treated cells are significantly greater than the untreated, but normal and cancer do not show significant differences.

From the treated and untreated mean fluorescence, the percent change was calculated as shown below:

$$\text{Percent Change} = 100 * \frac{(\text{Treated intensity} - \text{Untreated intensity})}{\text{Untreated intensity}}$$

Figure 3.5 shows the mean percent change for all six cell lines. The error bars represent standard deviations. Malignant cells have larger standard deviations than the normal. This figure shows that malignant cells have a significantly greater percent change than the normal cell lines (as denoted by the asterisks over the bars). The mean percent change in fluorescence is not significantly different in the different malignant cell lines, but is significantly different between the normal cell lines. The percent change in fluorescence from control is a useful method for delineating malignant cells from normal and could be exploited in breast cancer if incubation time in the drug can be decreased. Currently, our group is examining the spectral data obtained from these six cell lines to see if malignant cells can be demarcated after treatment with ALA without requiring information about endogenous fluorescence of control tissue as the fluorescence intensity images do.

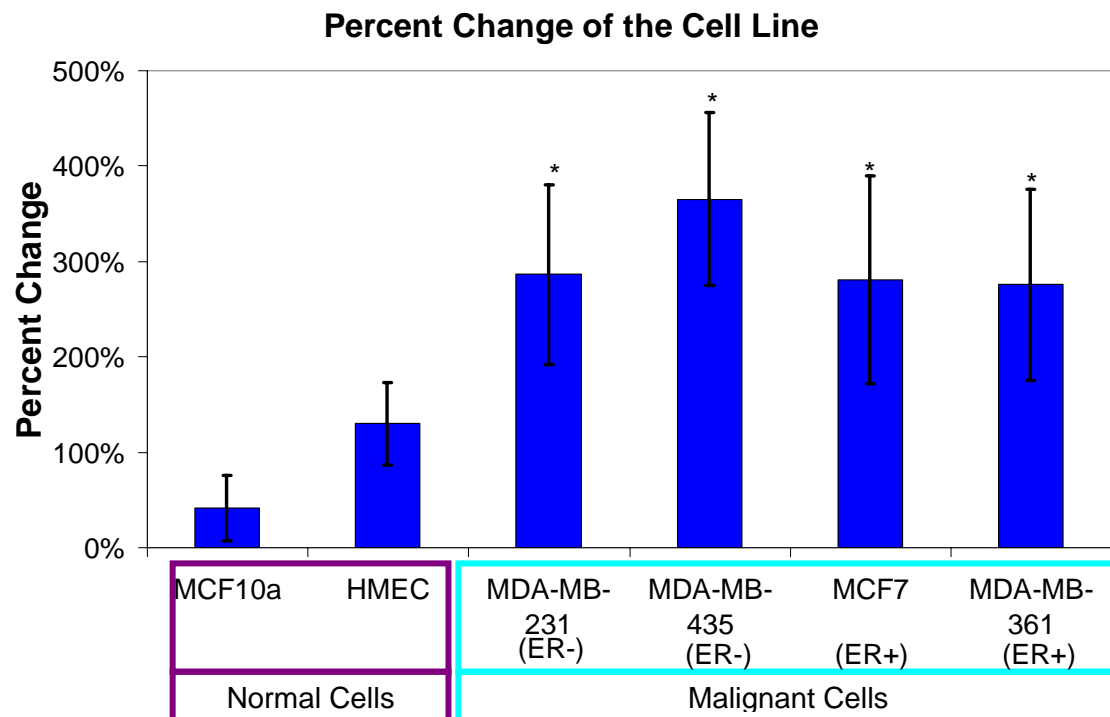


Figure 3.5. Average and standard deviation of the percent change in cellular fluorescence within each image. Astrisks denote that each malignant cell line is significantly different than the either normal cell line.

### 3.1.3 2-NBDG as a Contrast Agent

In the early portion of the year, PpIX was successfully used to discriminate malignant from normal cells. However, the kinetics of the pro-drug required a long incubation time, upwards of 2 hours, was necessary to induce large differences in fluorescence and a baseline fluorescence measurement was required. It was concluded that for clinical use within the operating room, PpIX is not ideal.

(2-NBDG) is a fluorescent analog of 2-Deoxy-2-[ $^{18}\text{F}$ ]fluoro-D-glucose ([ $^{18}\text{F}$ ]FDG), which has been used clinically in positron emission tomography (PET) for years [10]. 2-NBDG utilizes the GLUT transporters on the cell, the same way FDG does. 2-NBDG demonstrates the same malignant specificity as FDG does, but is safer for the patient and clinician. 2-NBDG, unlike FDG, is non-radiative and can be detected in the visible wavelength range. It is excited between 400-500 nm and its peak emission is at 540 nm. Previous studies of this compound have demonstrated its preferential uptake in the MCF-7 epithelial mammary cancer cell line over M-1 normal epithelial cells[10]. Our studies expand on this by optimizing 2-NBDG excitation in cells and examining different receptor status mammary cancer cell lines (six cell lines).

#### A. Cell Study Design

The MCF7 mammary cancer cell line has previously been shown to uptake 2-NBDG with fluorescence imaging microscopy [10, 11] and was therefore utilized to optimize imaging parameters prior to examination of further cell lines. A spectral confocal microscope was used for all cellular imaging.

The confocal microscope has various excitation wavelengths, which were tested for maximal 2-NBDG fluorescence excitation. The MCF7 cells were washed with phosphate buffer saline (PBS) twice and treated with 100  $\mu$ M of 2-NBDG dissolved in glucose-free D-MEM media (Gibco, California, USA) and incubated for 20 minutes. They were then washed again with PBS to remove the fluorescent 2-NBDG compound from the extra cellular space. This protocol was previously established in literature[11]. The same cell plates were then excited at differing excitation wavelengths to determine optimal excitation. The mean fluorescence intensity from the images was calculated and is shown in Figure 3.6. The error bars represent standard error. Student t-tests were conducted to test significant differences between the fluorescence intensity ( $p < 0.05$  was judged as significant). The 488 nm laser line was chosen because of its small standard deviation and higher fluorescence intensity and is used for all experiments following, although it was not quite significantly different from the 476 nm ( $p = 0.07$ ) wavelength.

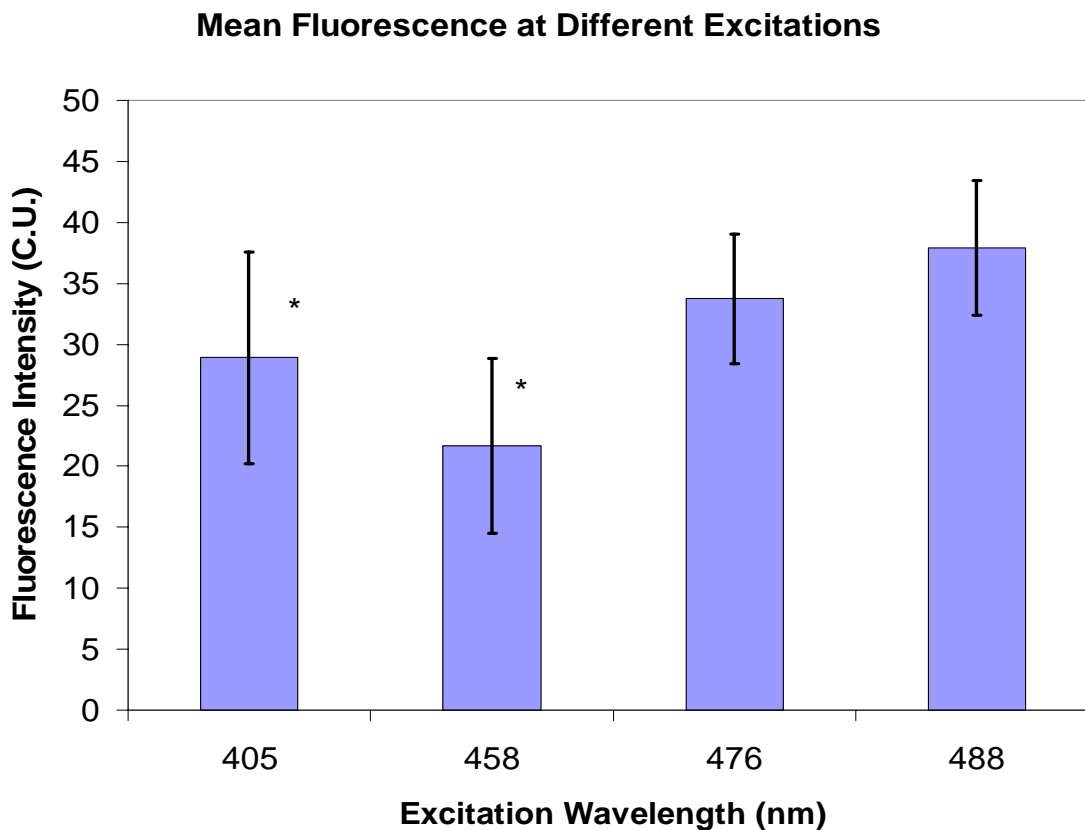


Figure 3.6: MCF7 fluorescence intensity at differing excitations of light. Asterisks denote statistical difference from the 488 nm laser line.

Concentration and incubation times were also optimized with the MCF7 cell line. Four different concentrations were compared to the control cells; 25, 50, 100 and 200  $\mu$ M. Control cells underwent the same steps as the treated cells, but were incubated in glucose-free D-MEM media without 2-NBDG for 20 minutes. Figure 3.7 shows the mean fluorescence intensity measured as a function of the different 2-NBDG concentrations. The bars represent standard error.

All concentrations showed a significant increase over the control cells ( $p < 0.01$ ) as determined by a Student's t-test. However, 100  $\mu$ M shows a small variance and still had an increase of over 200% from the control. Therefore, 100  $\mu$ M was chosen for testing cells.

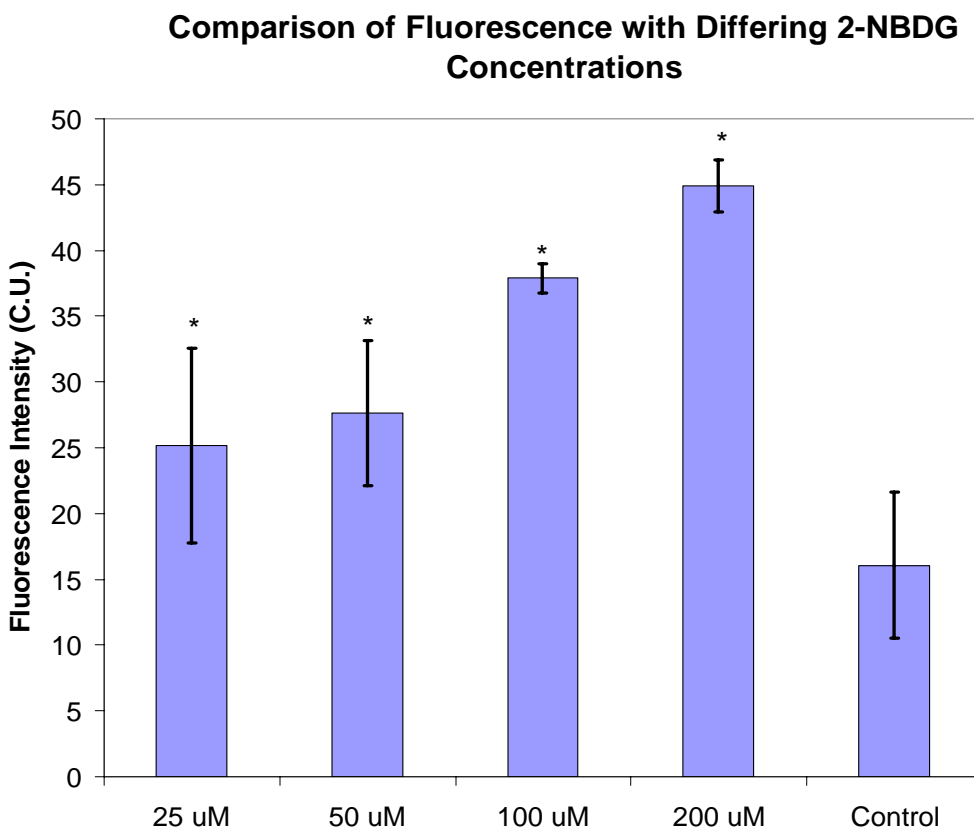


Figure 3.7. Mean fluorescence intensity with differing concentrations of 2-NBDG. Asterisks denote significant differences from the control.

Finally, incubation time was optimized to find the shortest time that effectively shows changes in fluorescence at 100  $\mu$ M concentration. Three different time points were chosen: 10, 20, and 45 minutes. All times showed significant differences with fluorescence intensity increasing with incubation time, but after consulting clinical staff 20 minutes was chosen since that is the longest time feasible in a clinical operating room (data not shown).

After the optimization of these parameters mean fluorescence intensity was calculated for five of the six cell lines used in the ALA study. However, several changes from the ALA study protocol were made. MCF10A, normal cell line, was replaced with a different malignant line, T47D. Also, the number of plates tested in this study was decreased to 4 because we were able to find significant differences over four plates.

The mean fluorescence intensity found for the 2-NBDG treated and control cell lines is shown in Figure 3.8. The error bars represent standard deviation between samples. Cells treated with 2-NBDG have significantly higher fluorescence intensities than untreated cells. This has been seen in previous literature [10]. It should be noted that the treated malignant cells are significantly higher than the HMEC normal cell line. Also, the malignant cells have differing receptor status, which does not appear to influence the uptake of the 2-NBDG when examining the raw fluorescence.

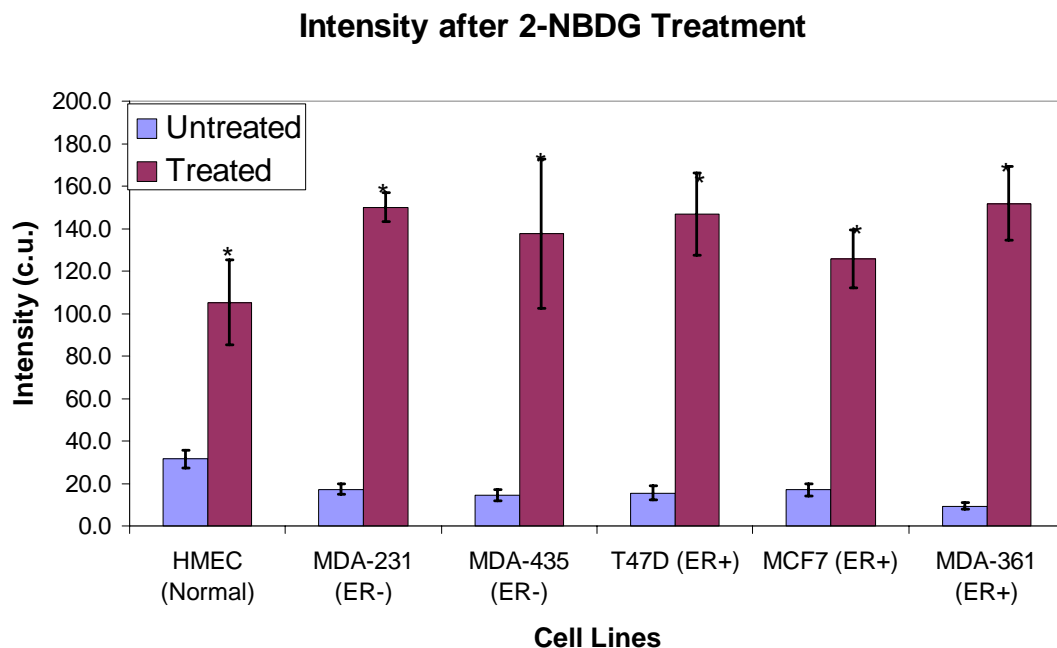


Figure 3.8. Mean fluorescence intensity of cells of varying receptor status as compared to a normal breast cell. Asterisks denote significant differences between the treated and untreated cell lines.

Figure 3.9 shows the mean percent change calculated from the mean fluorescence data from the same equation used to calculate the percent change in PpIX. The error bars represent standard error. From this figure, it is easy to distinguish that 2-NBDG accumulates more in malignant cells than in normal cells. This large differential change produced by 2-NBDG shows that 2-NBDG has great potential as a way to delineate malignant from normal with or without the baseline comparison. The baseline measurements would be a good way to examine endogenous fluorescence information on the untreated tissue, such as analyzing FAD levels of different metabolically active cells to see how it affects fluorescence uptake.

### Percent Change after 2-NBDG Treatment

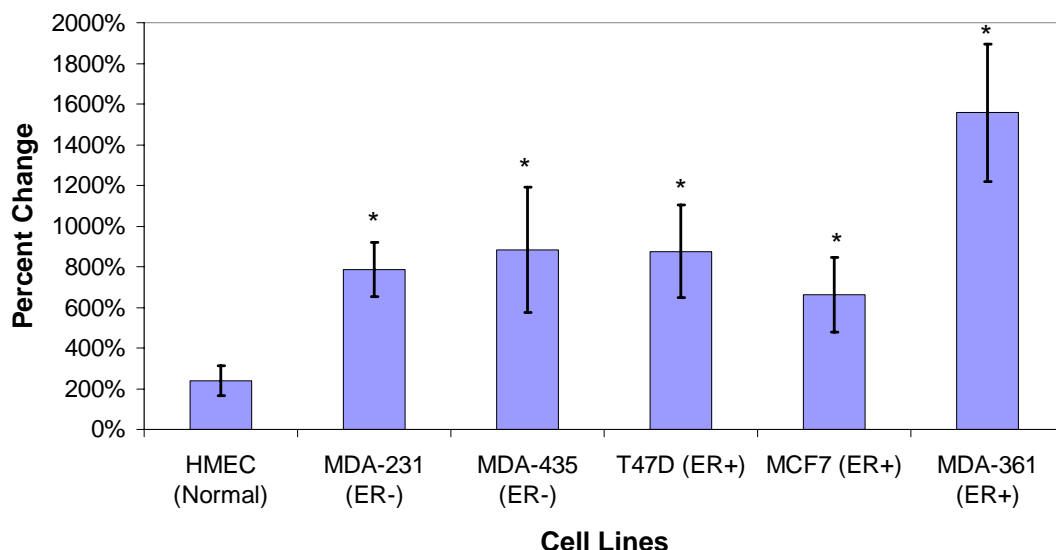


Figure 3.9. Mean percent change in fluorescence intensity of cells of varying receptor status as compared to a normal breast cell. Asterisks denote significant differences between normal (HMEC) and malignant cell lines.

#### Future Plans for years 4 and 5

Future studies with 2-NBDG will increase the number of cell lines to include another normal, MCF12, and utilize animal clinical models to help determine its applicability in ex vivo margin assessment for breast cancer. Ex vivo breast cancer tumors will be obtained from rats and the ability of 2-NBDG to diffuse through the system will be assessed with fluorescence microscopy and corresponding histology.

## 4. KEY RESEARCH ACCOMPLISHMENTS

### Project 1. System-on-a-chip device

- Successfully modified the probe geometries of the single-pixel probe developed in year 2 in order to increase the signal-to-noise ratio of the probe and to be able to extract a much larger range of optical properties than those of the probes built in year 2. The
- Validated new probe by testing in synthetic tissue phantoms over a wide range of absorption and reduced scattering coefficients
- Using the same phantom data collected by the new probe, optical properties with a reduced number of wavelengths were extracted to assess the feasibility of replacing the tunable light source with several smaller LEDs to further reduce the size and cost of the current system.
- Cross-talk analysis was performed as a first step to multiplex the single pixel system into an imaging system that can quantify tissue physiological and morphological properties over a large tissue area.
- Fabricated a 3x3 fiber-photodiode array for laboratory testing

## Project 2.

- Non-invasive optical measurements of diffuse reflectance can provide accurate estimates of tumor hypoxia.
- Another aspect of this project examined six breast cell lines and determined that PpIX production differs within the same cancer system, which has previously not been seen.
- PpIX discrimination requires a knowledge of endogenous fluorescence of the tissue.
- 2-NBDG can discriminate malignant breast cell lines from normal without an a priori knowledge of endogenous fluorescence in the tissue.

## 5. REPORTABLE OUTCOMES

### Project 1. System-on-a-chip device

- I. Lo JY, Yu B, Palmer GM, Kuech TF, Ramanujam N, "A Miniature Optical Device for Noninvasive, Fast Characterization of Tumor Pathology," 2008 OSA Topic Meeting in Biomedical Optics, March 16-19, 2008, St. Petersburg, Florida.
- II. Yu B, Lo JY, Palmer GM, Bender JE, Kuech TF, Ramanujam N, "A Cost-Effective Diffuse Reflectance Spectroscopy Device for Quantifying Tissue Absorption and Scattering In Vivo," *Journal of Biomedical Optics Letters*. Under Revision.
- III. Yu B, Fu H, Bydlon TM, Bender JE, Ramanujam N, "A Self-Calibrating Fiber Optic Probe for Tissue Optical Spectroscopy," CLEO 2008, May 6-8, 2008, San Jose, CA.
- IV. Lo JY, Yu B, Fu H, Bender JE, Palmer GM, Kuech TF, Ramanujam N. "A strategy for quantitative spectral imaging of tissue absorption and scattering using lightemitting diodes and photodiodes." *Optics Letters*. In preparation 2008.

### Project 2. Exploiting, physiological, metabolic and molecular contrast in breast cancer

- V. Millon SR, Provenzano PP, Elicieri, KW, Brown, JQ, Keely, PJ, Ramanujam, N. "Imaging of ALA-induced PpIX in normal and malignant breast cells". ECI (2007).
- VI. Vishwanath K, Yuan H, Moore L, Dewhirst M, Ramanujam N. "Optical Spectroscopy: an In Vivo, Non-invasive and Quantitative Technique for Assessing Tumor Response to Treatments." *Cancer research* 2008;(submitted).
- VII. Vishwanath K, Yuan H, Moore LK, Bender JE, Dewhirst M, Ramanujam N. "Longitudinal Monitoring of 4T1-Tumor Physiology *in vivo* with Doxorubicin Treatment via Diffuse Optical Spectroscopy," Optical Society of America: Biomedical Optics Topical Meeting, St. Petersburg, FL, Mar., 2008.
- VIII. Palmer GM, and Ramanujam N. "Monte Carlo based model for the extraction of intrinsic fluorescence from turbid media." *J Biomed Opt.* 13(2): p. 024017-9, 2008.

## 6. CONCLUSIONS

### Project 1

In year 3, we have modified the probe geometries of the single-pixel probe developed in year 2 in order to increase the signal-to-noise ratio of the probe and to be able to extract a much larger range of optical properties than those of the probes built in year 2. The new probe was tested in synthetic tissue phantoms over a wide range of absorption and reduced scattering coefficients, and the phantom optical properties were extracted from the diffuse reflectance spectra obtained from the tunable light source and new probe with the inverse MC model previously developed by our group. Using the same phantom data collected by our new probe, optical properties with a reduced number of wavelengths were extracted to assess the feasibility of replacing the tunable light source with several smaller LEDs to further reduce the size and cost of the current system. In addition, cross-talk analysis was performed as a first step to multiplex the single pixel system into an

imaging system that can quantify tissue physiological and morphological properties over a large tissue area. We have also fabricated a 3x3 fiber-photodiode array for test in the lab.

## Project 2

### **Predicting the validity of optical biomarkers to quantitatively and longitudinally monitor tumor hypoxia and necrosis in murine tumor models:**

Given these results, we can conclude that the estimated values of the deoxygenated hemoglobin concentration and mean reduced scattering coefficient from the diffuse reflectance spectra provide optical analogues of tissue hypoxia and necrosis, respectively. Further, the non-invasive nature of the optical techniques allowed us to estimate the changes in tumor hypoxia and necrosis over time, in each animal. Overall, we found that the tumors in the treated animals were better oxygenated than the tumors in the control animals. Though tumor necrosis increased slowly in the treated group over the first few days, we speculate that the cell kill occurred in the treated group because of treatment, while it occurred in the control group due to normal tumor growth.

### **2-NBDG and ALA as a Contrast Agents:**

The addition of exogenous aminolevulinic acid (ALA) can induce an excess of production of protoporphyrin IX (PpIX). This differential increase in fluorescence can be used to discriminate malignant breast cell lines from normal breast cell lines regardless of estrogen receptor status. A fluorescence increase of greater than 150% was seen in malignant breast cell lines as compared to normal breast cell lines. However, the long incubation time and the requirement of an a priori knowledge of the endogenous fluorescence, specifically the overlapping FAD signal, can be prohibitive for the use of ALA-induced PpIX fluorescence clinically. Alternatively, our group has shown that 2-NBDG, a fluorescent glucose analog, can be utilized to discriminate malignant breast cells of differing receptor status from normal breast cell lines with or without knowledge of the endogenous fluorescence signals to produce at least a 300% increase in malignant cell line fluorescence.

## 7. REFERENCES

1. Yu, B. and N. Ramanujam, *A Cost-Effective Diffuse Reflectance Spectroscopy Device for Quantifying Tissue Absorption and Scattering In Vivo*. Opt Lett, 2008.
2. Zhu, C., Palmer GM, Breslin TM, Harter JM, Ramanujam N, *Diagnosis of Breast Cancer using Fluorescence and Diffuse Reflectance Spectroscopy: a Monte Carlo Based Approach*. J Biomed Opt, 2008. **13**(3): p. 034015.
3. Palmer, G.M. and N. Ramanujam, *Monte Carlo-based inverse model for calculating tissue optical properties. Part I: Theory and validation on synthetic phantoms*. Appl Opt, 2006. **45**(5): p. 1062-71.
4. Baumann, M., C. Liertz, H. Baisch, T. Wiegel, J. Lorenzen, and H. Arps, *Impact of overall treatment time of fractionated irradiation on local control of human FaDu squamous cell carcinoma in nude mice*. Radiother Oncol, 1994. **32**(2): p. 137-43.
5. Appold, S., M. Baumann, C. Petersen, K. Horn, and F. Eichhorn, *Comparison of the response of human FaDu squamous cell carcinoma in nude mice after hypofractionated-accelerated regimens and "curative" fractionation schedules*. Strahlenther Onkol, 1998. **174**(6): p. 315-9.
6. Yaromina, A., T. Holscher, W. Eicheler, A. Rosner, M. Krause, F. Hessel, C. Petersen, H.D. Thames, M. Baumann, and D. Zips, *Does heterogeneity of pimonidazole labelling correspond to the heterogeneity of radiation-response of FaDu human squamous cell carcinoma?* Radiother Oncol, 2005. **76**(2): p. 206-12.
7. Yaromina, A., D. Zips, H.D. Thames, W. Eicheler, M. Krause, A. Rosner, M. Haase, C. Petersen, J.A. Raleigh, V. Quennet, S. Walenta, W. Mueller-Klieser, and M. Baumann,



- Pimonidazole labelling and response to fractionated irradiation of five human squamous cell carcinoma (hSCC) lines in nude mice: the need for a multivariate approach in biomarker studies.* Radiother Oncol, 2006. **81**(2): p. 122-9.
8. Yaromina, A., M. Krause, H. Thames, A. Rosner, F. Hessel, R. Grenman, D. Zips, and M. Baumann, *Pre-treatment number of clonogenic cells and their radiosensitivity are major determinants of local tumour control after fractionated irradiation.* Radiother Oncol, 2007. **83**(3): p. 304-10.
  9. Gibbs, S.L., B. Chen, J.A. O'Hara, P.J. Hoopes, T. Hasan, and B.W. Pogue, *Protoporphyrin IX level correlates with number of mitochondria, but increase in production correlates with tumor cell size.* Photochem Photobiol, 2006. **82**(5): p. 1334-41.
  10. O'Neil, R., L. Wu, and N. Mullani, *Uptake of a fluorescent deoxyglucose analog (2-NBDG) in tumor cells.* Molecular Biology, 2005. **7**(6): p. 388-392.
  11. Cheng, Z., J. Levi, Z. Xiong, O. Gheysens, S. Keren, X. Chen, and S.S. Gambhir, *Near-infrared fluorescent deoxyglucose analogue for tumor optical imaging in cell culture and living mice.* Bioconjug Chem, 2006. **17**(3): p. 662-9.
  12. Masilamani, V., K. Al-Zhrani, M. Al-Salhi, A. Al-Diab, and M. Al-Ageily, *Cancer diagnosis by autofluorescence of blood components.* Journal of Luminescence, 2004. **109**(3-4): p. 143-154.
  13. Meng, J.W., X.J. Wang, H.P. Ma, X.G. Ren, X.R. Xu, and W.M. Ren, *Protoporphyrin IX fluorescence from the plasma of tumor-implanted mouse.* Journal of Luminescence, 1999. **83-4**: p. 251-254.